2015

An Investigation of the Effect of MN2+ on the FTH1 IRE-IRP Complex

Eric Thomas Mendenhall
mendenhall8@marshall.edu

AN INVESTIGATION OF THE EFFECT OF MN^{2+} ON THE FTH1 IRE-IRP COMPLEX

A thesis submitted to
the Graduate College of
Marshall University
In partial fulfillment of
the requirements for the degree of
Master of Science
in
Chemistry
by
Eric Thomas Mendenhall
Approved by
Dr. Bin Wang, Committee Chairperson
Dr. Michael Norton
Dr. Leslie Frost

Marshall University
May 2015

ACKNOWLEDGEMENTS

Cody Harrison and Leesah Al-Qawasmi- Assistance with hSHAPE chemistry experiments.

Joshua Botkin- Assistance with AFM experiments.

Christian Warner- Synthesized G3 Dendron and other AFM reagents.

Andrea del Pilar Belalcazar- Obtained protocol to synthesize working IRP protein.

William Patterson III- Continued synthesis of several reagents for all experiments, maintaining cell culture line and for daily lab assistance and support when needed.

Dr. Scott Day and Masudur Rhaman- Both were integral in providing the construct and idea for the DNA Dendron for the AFM experiment.

David Neff and the Norton Lab Group- For assistance and allowing me allotted time in their busy schedule to step in and use their AFM. A special thanks to David for his continued assistance and support during all aspects of the AFM experiments.

Dr. Michael Norton- For his great support and contributions in providing the idea to image the IRE/IRP complex using his AFM laboratory. Additional thanks for his expertise in providing the knowledge on AFM imaging techniques, and for helping to push the boundaries of AFM imaging for this research.

Dr. Bin Wang- A special thanks to Dr. Wang for being my thesis advisor and selecting me to work in her lab as a graduate assistant. Her many contributions to this research include everything involved in the EMSA and hSHAPE experiments. Her expertise in hSHAPE chemistry is top tier, and she provides a great deal of insight and knowledge in this subject. Additionally her continued support never goes unnoticed.

Additional thanks for this provided opportunity go to:

NSF RII IRT3 Grant EPS-1003907 for providing the funding for this research.

Marshall University Graduate College of Science and Dr. Charles Somerville.

Marshall University Department of Chemistry.

Lastly, none of this could have been accomplished without the full faith, love, and support of my family.

TABLE OF CONTENTS

List of Figures……. v

List of Graphs……..vi

List of Tables……..vii

Abstract……..viii

Chapter 1. Introduction……...…..1

1.1 Iron Homeostasis and Ferritin……1

1.2 IRP-IRE Complex and its Components……..2

1.3 Negative Effects on the IRP-IRE Complex……6

1.4 Electrophoretic Mobility Shift Assays……...10

1.5 Atomic Force Microscopy……..10

1.6 hSHAPE Chemistry……....12

Chapter 2. Experimental Methods……..……..16

2.1 DNA Synthesis……16

2.2 RNA Synthesis……17

2.3 IRP Synthesis…….....18

2.3.1 Plasmid Cloning and Purification…….18

2.3.2 Protein Over-Expression and Purification……19

2.4 EMSA Experiments…….20

2.4.1 IRE Comparative Gel……20

2.4.2 Metal Ion Titration Gel…….21

2.4.3 Mn^{2+} Pre-Incubation Experiments..……..22

2.5 hSHAPE Chemistry Experiments……23

2.5.1 Selective 2’ Hydroxyl Acylation……...23

2.5.2 Primer Extension……...24

2.5.3 Capillary Electrophoresis……..24

2.5.4 Data Analysis……25

2.6 AFM Experiments……....26

TABLE OF CONTENTS (CONT.)

Chapter 3. Experimental Results……...……...28

3.1 IRP-IRE Complex Formation EMSA Gel Experiment……..28

3.2 IRP-IRE Complex Formation hSHAPE Chemistry Experiments……..28

3.3 IRP-IRE Complex Formation AFM Experiments……..41

3.4 IRP-IRE Complex Dissociation EMSA Mn^{2+} Titration…….43

3.5 IRP-IRE Complex Dissociation by Mn^{2+} hSHAPE Experiments……..…45

3.6 EMSA Mn^{2+} Pre-Incubation Experiments…….…..…...51

Chapter 4. Discussion..…….54

Chapter 5. Conclusions..……...61

References..……..…….62

APPENDIX A: IRB LETTER OF APPROVAL……..……...65

LIST OF FIGURES

1. Ferritin Structure……2

2. IRP Dual Function and 4Fe-4S Cluster……..…..3

3. 5’ and 3’ Untranslated Region IREs……4

4. Binding Nucleotides of IRE to IRP……6

5. Mutant IRE Binding Affinity……...7

6. Metal Ion Influences on IRP-IRE Complex……8

7. Yohimbine Effects on IRP-IRE Complex……9

8. DNA Dendron Scaffold……...12

9. Selective 2’ Hydroxyl Acylation……13

10. Primer Extension……...14

11. DNA PCR Product……17

12. ABI 310 Genetic Analyzer……....25

13. Bruker Corporation Atomic Force Microscope…….26

14. EMSA IRE Comparative Gel……28

15. Predicted IRE Structure……31

16. Predicted IRE Structure with IRP……..34

17. Predicted Mutant IRE Structure…….37

18. Predicted Mutant IRE Structure with IRP……..40

19. AFM DNA Dendron Image……41

20. AFM DNA Dendron-IRE-IRP Image…….42

21. EMSA Mn^{2+} Titration…….43

22. Predicted IRE Structure with IRP in 50 µM Mn^{2+}.....46

23. Predicted IRE Structure with IRP in 500 µM Mn^{2+}……...48

24. Predicted IRE Structure with IRP in 5 mM Mn^{2+}……..50

25. EMSA Control Gels……...51

26. Pre-IRE and IRP Mn^{2+} Incubation Gel……...52

27. Pre-IRE only and Pre-IRP only Mn^{2+} Incubation Gel……52

28. Combined Pre-Incubation Experiments 3:1 EMSA Gel…….53

LIST OF GRAPHS

1. Raw Data Electropherogram of IRE……29

2. SHAPE Reactivity Histogram of IRE……...30

3. Raw Data Electropherogram of IRE with IRP……..32

4. SHAPE Reactivity Histogram of IRE with IRP……33

5. Raw Data Electropherogram of Mutant IRE……35

6. SHAPE Reactivity Histogram of Mutant IRE……...36

7. Raw Data Electropherogram of Mutant IRE with IRP……..38

8. SHAPE Reactivity Histogram of Mutant IRE with IRP……39

9. EMSA Mn^{2+} Titration Curve……44

10. SHAPE Reactivity Histogram of IRE with IRP in 50 µM Mn^{2+}……45

11. SHAPE Reactivity Histogram of IRE with IRP in 500 µM Mn^{2+}……...47

12. SHAPE Reactivity Histogram of IRE with IRP in 5 mM Mn^{2+}……..49

LIST OF TABLES

1. Sequences in DNA PCR Reactions……17

2. Standardized RNA Intensity Values of Mn^{2+} Pre-Incubation 3:1 EMSA Gel……...53

ABSTRACT

Iron is a widely distributed metal found in almost every physiological system in nature, thus being an essential part of life. Iron homeostasis in the human body must be tightly regulated as iron is both beneficial and harmful to different cellular processes. Ferritin is a protein that has a prominent role in maintaining iron homeostasis via iron sequestration. Additionally, this protein itself is regulated by the Iron Responsive Element (IRE) and its interaction with an apo-aconitase protein or the Iron Regulatory Protein (IRP). The binding of the IRP to this IRE, located on the 5' untranslated stem loop region of the ferritin mRNA, will inhibit translation into Ferritin creating an additional major mechanism to control cellular iron metabolism. Previous literature had indicated that divalent metal ions (Fe^{2+}, Mn^{2+}) and small molecule drugs can interrupt the binding of the IRE-IRP complex, specifically by altering the secondary structure of the IRE. Following this model, we conducted a series of experiments using Atomic Force Microscopy (AFM), Electrophoretic Mobility Shift Assays (EMSAs), and high-throughput Selective 2'Hydroxyl Acylation analyzed by Primer Extension (hSHAPE) Chemistry to observe effects from Mn^{2+} on already bound IRE-IRP complexes. The results concluded the Mn^{2+} had little to no effect on an already bound IRE-IRP complex. However upon changing our experimental procedure, EMSA experiments show pre-incubating the IRE and IRP separately in Mn^{2+} prior to binding affects complex formation. The results also indicated it is the IRP being affected by the Mn^{2+} and not the IRE, which contradicts the previous model.

CHAPTER 1

INTRODUCTION

1.1 Iron Homeostasis and Ferritin

Iron is a widely abundant metal found both in the surrounding environment, and in many bio-physiological systems, thus being an essential part of life. In the human body, Fe has several important roles such as its involvement in key redox reactions, integration into hemoglobin and myoglobin, or acting as a cofactor in metalloproteins that have significant parts in metabolism. On the contrary, Fe can also be a very potent ion in physiological systems. Iron's involvement in Fenton Reaction chemistry can result in a cascade of effects by reacting with hydrogen peroxide, yielding reactive oxygen species that proceed to damage several important systems in cells.

Therefore, it is imperative that Fe homeostasis be closely regulated in the body. One such way that Fe levels are regulated is through a series of iron binding proteins with the capabilities to transport, store, and excrete Fe in the cell. Such proteins include Ferroportin, which transports Fe across cellular membranes, Transferrin, which controls cellular Fe transportation, and Ferritin that is involved in Fe sequestration. The evolution of these proteins working in concert indicates that the human body does not have one distinct physiological pathway and that Fe regulation must be maintained by the collective effort of these mechanisms.

One of these proteins, Ferritin, is the focus of our research. This ubiquitous protein is found in higher plants, fungi, bacteria, invertebrates, and vertebrates. In vertebrates, Ferritin has a highly conserved primary structure.[1] It is a large protein (450,000 Da) with a 24 subunit protein cage that is in contact with an iron core. Fe travels to and from the core via the subunits assembled into four α-helical bundles (Figure1).[2] The subunits of Ferritin are divided into the heavy chain subunits (21,099 Da) and the light chain subunits (19,766) which are 55%

homologous.[1] The heavy chain subunit is responsible for ferroxidase conversion of the Fenton Chemistry reactive Fe^{2+} to a less reactive Fe^{3+}-O-Fe^{3+} complex, thus allowing ferritin to fulfill its role in Fe sequestration in an efficient manner.[3] The light chain subunit is involved in electron transfer across ferritin's protein cage and does not play a role in feroxidase conversions.[4]

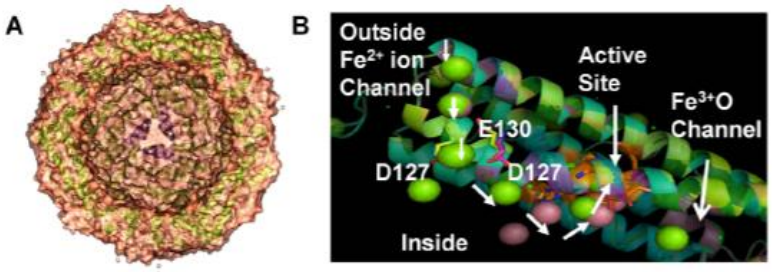

Figure 1. Ferritin Structure. (A) A cross-section of the ferritin protein cage with its core at the center. (B) Represents one of the subunits assembled into a four α-helical bundle. The white arrows represent the metal ion traffic in the subunit.[2]

1.2 IRP-IRE Complex and its Components

In addition to having a network of proteins to assist in controlling Fe homeostatic levels, several of these proteins themselves have their own control mechanisms through translational regulation via the Iron Regulatory Protein (IRP) – Iron Responsive Element (IRE) network. Each IRP-IRE network is comprised of two components: The Iron Regulatory Protein and a small stem loop region of mRNA known as the Iron Responsive Element. The IRP-IRE network has the ability to influence the production levels of several iron binding proteins, including ferritin, therefore this network has a direct effect on Fe homeostasis in the body.

The Iron Regulatory Protein is a dual functional protein that acts as both a cytosolic aconitase1 (ACO1) protein, and as the IRP when in its apo-ACO1 form.[5] When in the apo- form, IRP is capable of binding to IRE engaging in the IRP-IRE translational control (Figure 2A). When in the ACO1 form, the protein contains an iron-sulfur cluster (4Fe-4S).[6] This 4Fe-4S cluster specifically binds to three cysteine amino acids (Cys 437, Cys 503, and Cys506), and

gives the IRP its ability to perform its ACO1 activity (Figure 2B). The 4Fe-4S cluster is assembled in the mitochondria by scaffolding proteins. It is then brought to an apo-ACO1 via a specific transporter protein where it is inserted into the ACO1 giving it full aconitase activity. The metal cluster binds to the protein by three Fe-Cysteine bonds. The fourth Fe in the 4Fe-4S cluster is a labile Fe that is involved in the function of ACO1, which is the conversion of citrate to isocitrate in the citric acid cycle.[7] ACO1 also has the ability to lose this labile Fe leaving it with a 3Fe-4S cluster. When this occurs, the protein loses both its function as an aconitase, and as an IRP.

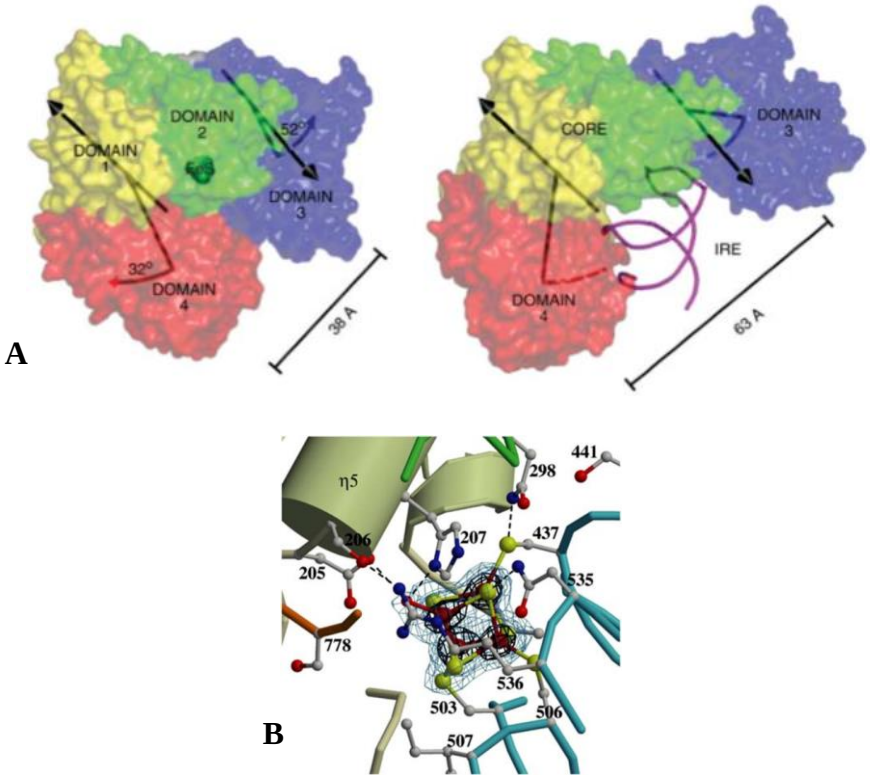

Figure 2. IRP Dual Function and 4Fe-4S Cluster. (A) This schematic represents the dual-functional ability of the IRP with and without the 4Fe-4S cluster. (B) An enhanced view of the 4Fe-4S cluster, and its binding locations to the IRP.[6,8]

Iron Responsive Elements are small non-coding, untranslated stem loop regions (UTRs) of various mRNAs encoding for several iron binding proteins (Figure 3). They can exist as either 3' UTRs or 5' UTRs. Translational regulation occurs from these loop regions through the complexing of the IRP with these IREs. When an IRP-IRE complex is formed on a 3' UTR, the mRNA is stabilized from endonuclease degradation. On the contrary, when an IRP-IRE complex is formed on a 5' UTR, translational repression occurs and less of that protein is produced.[9]

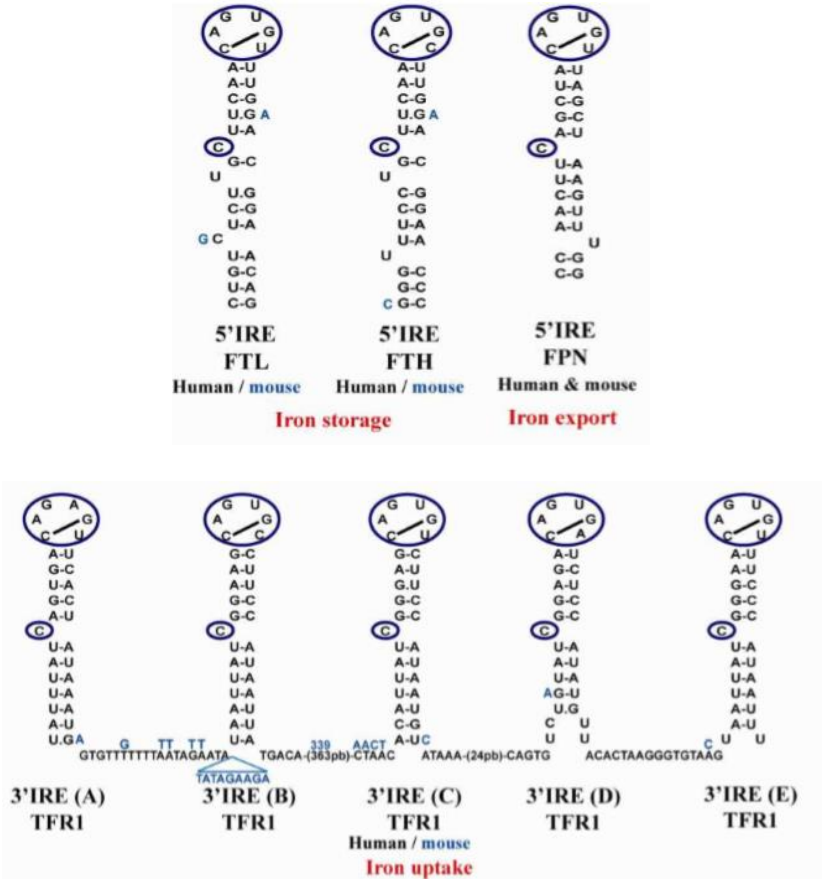

Figure 3. 5' and 3' Untranslated Region IREs. The FTH and FTL represent 5' loop regions for human heavy and light chain ferritin mRNA respectively. The blue nucleotides are in the mouse IRE. The FPN represents the 5' loop region in ferroportin mRNA. The five TFR1 3' loop regions are all found on the transferrin receptor mRNA.[9]

The IRP-IRE complex that we are studying in our experiments belongs to the 5'UTR of the Heavy Chain Human Ferritin (FTH1) mRNA. This complex helps to influence Fe homeostasis by controlling ferritin translation. When intracellular Fe levels drop below the physiological set-point, the 4Fe-4S cluster doesn't form as readily, thus leaving many apo-aconitase or IRPs in the cell. The IRP binds to the IRE of the FTH1 mRNA and represses the production of ferritin, therefore allowing Fe concentrations to restore to their set-point. However, when Fe levels are elevated, the 4Fe-4S complex more readily forms, meaning there are more ACO1 proteins in the cell than IRPs. With the lack of IRP binding to IRE, translation is able to occur as usual, producing Ferritin, which will in turn, fulfill its role by sequestering the excess Fe and relieving the stress of elevated Fe levels.

Previous research has given rise to the resolved crystal structure of double mutant Rabbit IRP in complex with Frog heavy chain ferritin IRE. Being that this IRE is fairly conserved across species, the IRP domains which have multiple interactions with specific nucleotides of the IRE can be identified (Figure 4).[8] From the figure it can be seen that the major binding locations of the IRP-IRE complex are located on the C8, A15, G16, and U17 nucleotides of the IRE. All of these nucleotides are conserved in the Human IRE sequence as well.

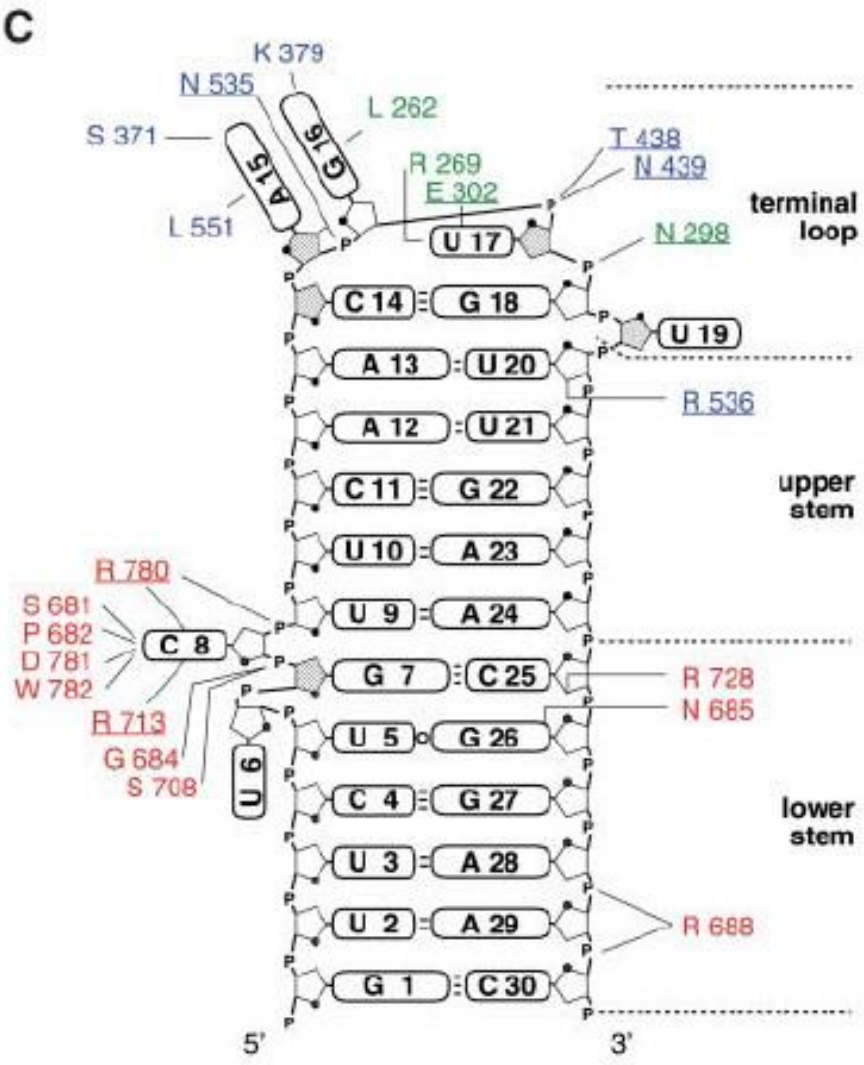

Figure 4. Binding Nucleotides of IRE to IRP. These locations were determined by x-ray crystallography. The key nucleotides in binding, C8, A15, G16, and U17 are all shown to have multiple interactions with the IRP. The C8 bulge has the most IRP interactions binding with six different amino acids and eight amino acids total.[8]

1.3 Negative Effects on the IRP-IRE Complex

Mutations in one or several of these nucleotides in the sequence could affect the binding of the IRP-IRE complex. One point mutation in particular is an A15U mutation in the stem loop region that, as described above, is in direct binding contact with the IRP. This mutation was found to cause decreased binding affinity of the IRP to the mutant IRE (Figure 5).[10]

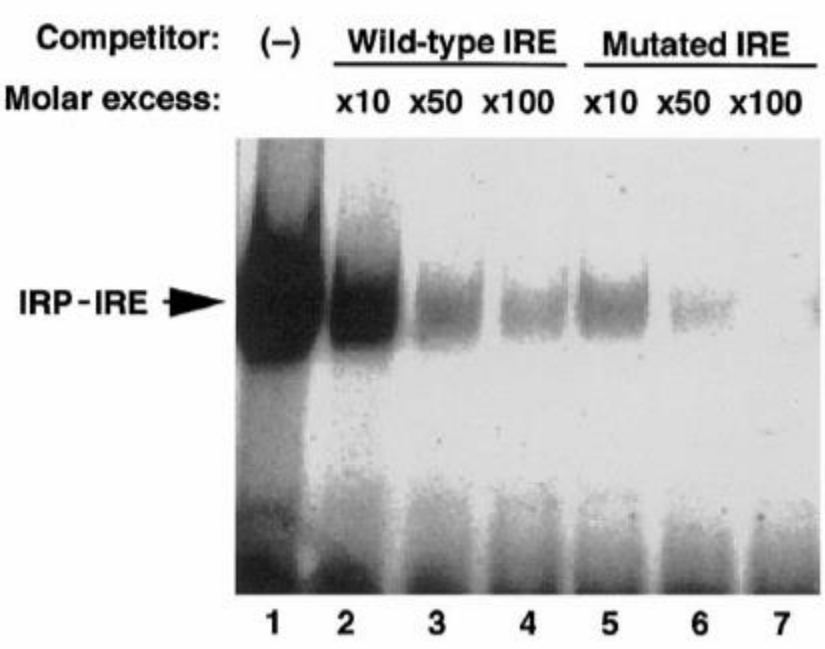

Figure 5. Mutant IRE Binding Affinity. This represents a band-shift assay from the Kato group, comparing the mutant and wild-type IREs when bound to IRP.[10]

It is quite evident from this experiment that the mutated IRE has a much weaker binding affinity for the IRP than the wild-type. This decreased affinity can be seen in the decreased fluorescence of the IRP-IRE bands, the upper bands in the gel.

Another effector to the IRP-IRE complex completely unrelated to genetic mutations, and the focus of our experimental investigations, is the effect of divalent metal ions (Fe^{2+} and Mn^{2+}) and small molecule drugs on the complex. The model we are testing was previously formulated by the Khan group and resulted from studies in which they demonstrated metal ions having a direct influence on IRP-IRE complex formation and dissociation.[11,12] Figure 6B shows the direct effect of Fe^{2+} on complex formation observed through the decreased intensity in the "RNA + Protein" bands of the right-hand gel. In this same study, the group conducted fluorescence intensity experiments where upon UV illumination, IRE decreased in intensity whereas IRP did

not, leading to their conclusion that the metal ions Mn^{2+} and Mg^{2+} have a direct effect on the IRE of the complex, and not the IRP (Figure 6A).[11]

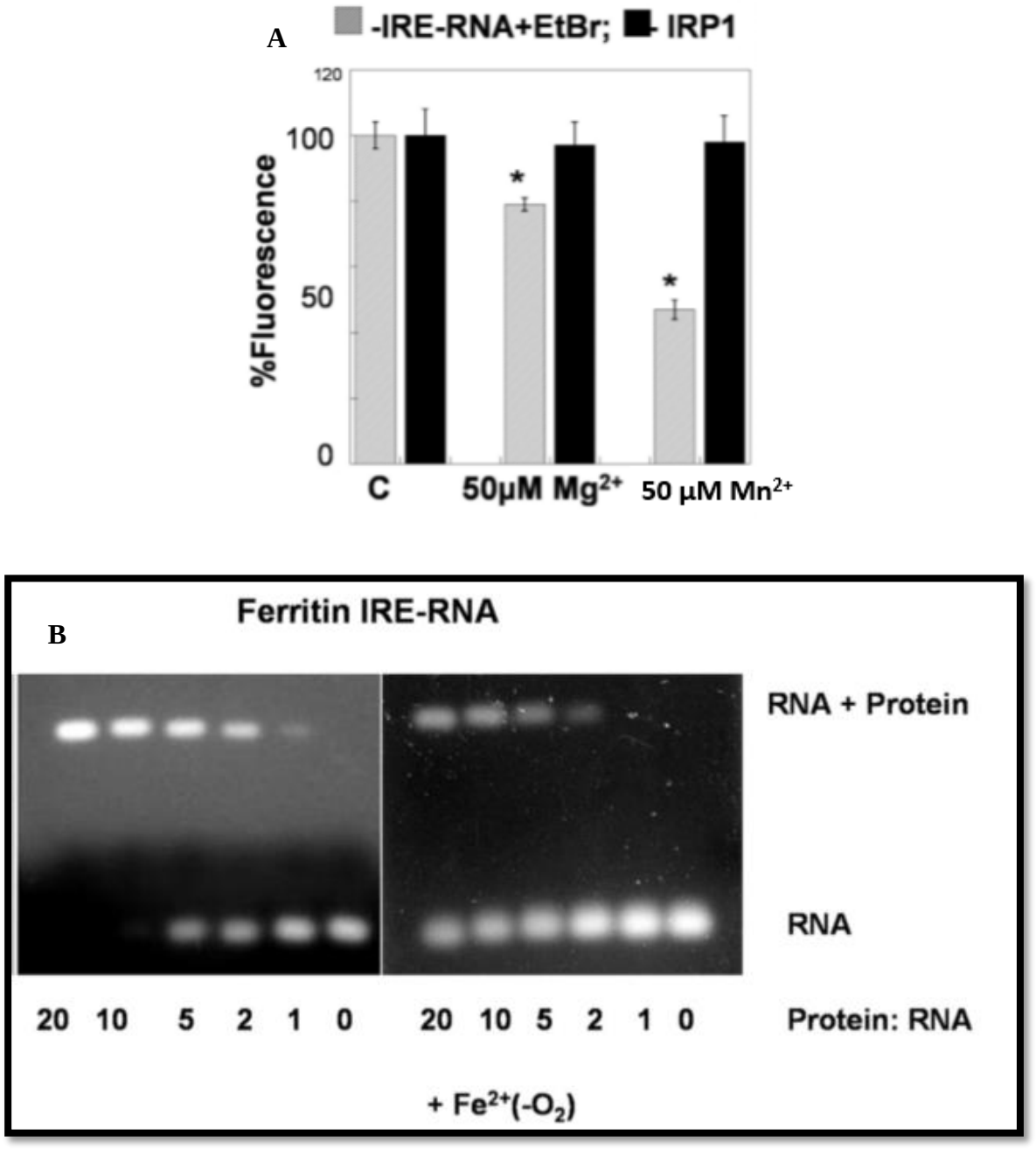

Figure 6. Metal Ion Influences on IRP-IRE Complex. (A) Results of a fluorescence intensity study of the IRE and IRP. The IRE was incubated with metal ions and then ethidium bromide. The IRP was interacted with metal ions only. (B) EMSA gels from the same group showing the result of IRP-IRE complex formation with and without the interaction of Fe^{2+}.[11]

Additional studies by other groups suggest that small molecule drugs have analogous effects on the complex as the divalent metal ions. One such study shows the direct effect on the IRP-IRE complex by the small molecule drug yohimbine, a drug used for many medical applications (Figure 7).[13] The experiment shows the small effect that yohimbine has on the dissociation of the complex. As the concentration of the yohimbine was increased, dissociation of the complex also increased. The resultant dissociation can also be observed in the percentages of the bound vs. total (bound plus unbound) RNA in the bar graph on the right. Another study demonstrated the interactions of anthracyclines (doxorubicin and daunorubicin) with the IRE.[14] Being that these anthracyclines are clinically useful chemotherapeutic drugs, there are heavy implications involved in the side effects on the IRP-IRE complex.

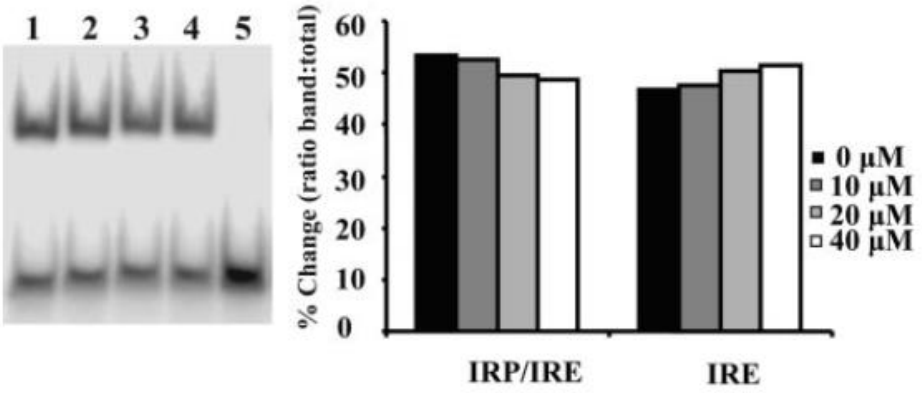

Figure 7. Yohimbine Effects on IRP-IRE Complex. Results of IRP-IRE studies with yohimbine are shown above. From the EMSA gel, yohimbine lane concentrations are as follows: 1=0uM, 2=10uM, 3=20uM, 4=40uM.[13]

Therefore, the objective of our study is to focus on the divalent metal ions (Fe^{2+} and Mn^{2+}), and observe their direct effects on the IRP-IRE complex following the Khan model. Our lab used three different techniques to characterize the complex under such effects. The first was electrophoretic mobility shift assays (EMSAs). The EMSA gels were used to observe both the

IRP-IRE complex formation and Mn^{2+} influences on complex formation and dissociation. The second technique that was implemented was Atomic Force Microscopy (AFM). This technique allowed us to detect complex formation and dissociation based on observational z-height differences. Lastly, our most sensitive technique, high-throughput selective 2' hydroxyl acylation analyzed by primer extension (hSHAPE) chemistry, allowed us to discern, nucleotide by nucleotide, any modifications made to the secondary structure of the IRE RNA under various conditions.

1.4 Electrophoretic Mobility Shift Assays

EMSAs are a common technique to study RNA-protein interactions.[15,16] Molecules of different weights and charges are separated as they migrate through the gel at different speeds. A current is applied to the gel allowing more negatively charged molecules and/or smaller molecules to migrate toward the positively charged electrodes at higher speeds. The percentage of agarose in the gel dictates the speed at which molecules will migrate. The higher the percentage the more separation will occur between molecules of different sizes.

The EMSA gels used in our experiments provided the ability to observe the separation between RNA bound in the IRP-IRE complex, and unbound RNA which was not in the complex. Additionally, we used the resultant images from these gels to quantify the amount of RNA bound and unbound which could be used to determine effects on the complex from either metal ions or small molecule drugs.

1.5 Atomic Force Microscopy

AFM is a highly sensitive microscopy technique that is able to provide its users with physical representations of small biomolecules on the nanometer scale. Some instruments are

capable of discerning molecules in the Angstrom range and one group has even been able to achieve the imaging and characterization of molecular bonds using CO modified tips.[17,18] AFM is a common technique for molecular biochemists, and has been used quite often to image both single and double stranded nucleic acids with high resolution.[19,20]

Therefore, this technique would be very appropriate in attempting to characterize our IRE RNA and IRP upon complexation. Our approach would be to build the complex upon a scaffold and observe increased changes in z-heights upon additions by each component of the complex. Then we would introduce known complex disruptors, such as the metal ions, and observe any decreased changes in z-height, indicating complex dissociation.

The concept for the scaffold used to image our IRP-IRE complex was derived from previous DNA dendrimer experiments.[21] The concept of the DNA dendrimer scaffold allows for an anchored complimentary DNA strand, which would be ideal for AFM imaging techniques (Figure 8). Each dendrimer head is cut in half to form DNA dendrons. These dendrons have branches containing thioacetate groups, and when reacted with hydroxylamine, reveal exposed thiolated branches that will bind with a high affinity to gold surfaces. There is a complimentary single stranded DNA tail that is left unbound to the surface, and exposed for interactions with RNA. Therefore our construct is a thiolated DNA dendron on a gold surface, followed by the binding of the IRE RNA and lastly the IRP. Upon each subsequent addition to our construct, changes in z-height are to be observed, and recorded by the AFM.

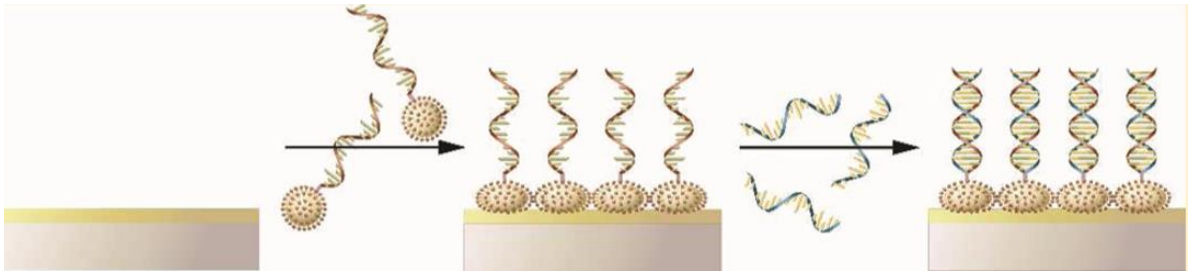

Figure 8. DNA Dendron Scaffold. Upon AFM imaging the DNA dendrons, the thiolated dendron head is what gets detected by the AFM tip and the small strand of DNA is not observed.[21]

1.6 hSHAPE Chemistry

Lastly, our most sensitive technique used to characterize our IRP-IRE complex is hSHAPE chemistry. This technique provides us with a nucleotide by nucleotide two dimensional interrogation of our IRE with high accuracy.[22,23] Essentially any resultant structural modifications made to the IRE during any of the experimental procedure will be detected with this technique. As mentioned in section 1.3, hSHAPE is an acronym: high-throughput selective 2'-hydroxyl acylation analyzed by primer extension. This name represents the several processes involved in hSHAPE chemistry.

The first process is the selective 2'hydroxyl acylation. In this step, a nucleophile reacts with the 2'-hydroxyl group on RNA to form a bulky esterification 2'-O-adduct. This adduct will react with higher probability to the RNA when the 2'-hydroxl group is exposed (unconstrained) and not destabilized by the oxygen on the 3'-phosphate group (Figure 9).[24] The exposed 2'-hydroxyl groups are generally located in single stranded nucleotides of the RNA. Base paired nucleotides, or nucleotides undergoing tertiary interactions will have constrained 2'hydroxyl groups, and therefore remain fairly unreactive with the nucleophile.

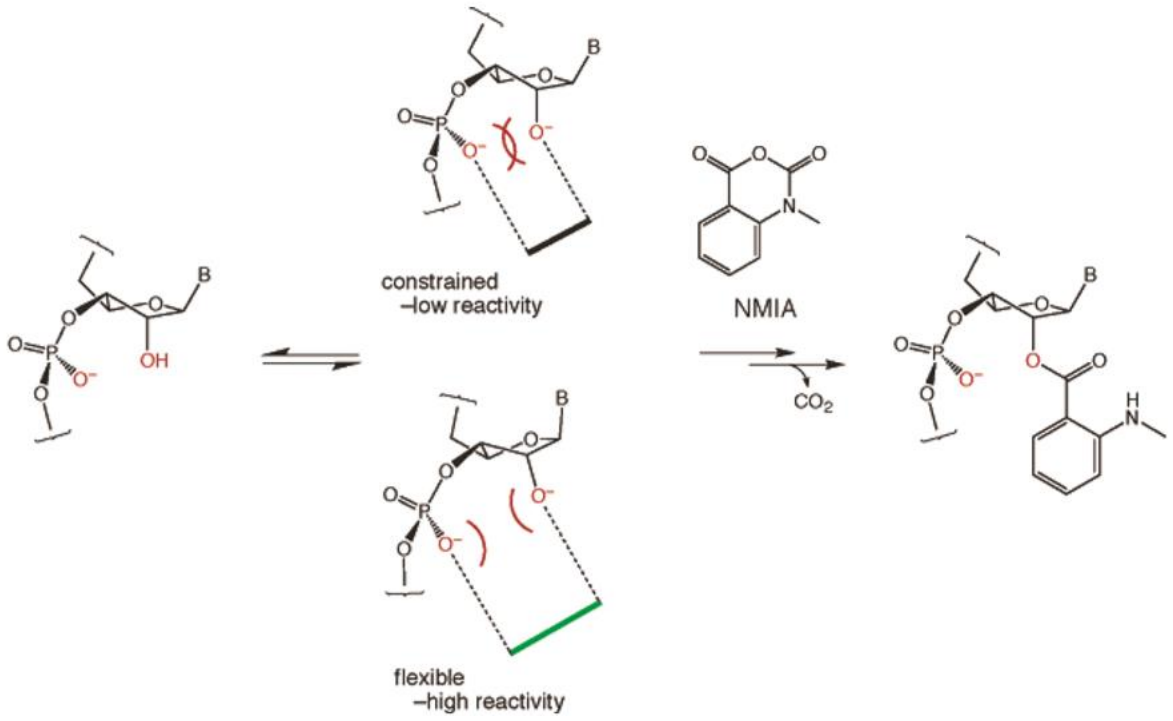

Figure 9. Selective 2' Hydroxyl Acylation. Representation of the selective 2' hydroxyl acylation reaction. The nucleophile used in this figure is N-methylisatoic anhydride (NMIA), however experiments here use 1-methyl-7-nitroisatoic anhydride (1M7).[24]

The bulky adduct contributes to the second process of hSHAPE chemistry, which is the analysis by primer extension. The primer extension occurs by a reverse transcription reaction that yields fluorescently labelled cDNA. The nucleotides that contain the 2'-O-adducts are detected as stops to the reverse transcriptase enzyme (Figure 10).[25] This reaction yields fluorescently labelled cDNA strands of several lengths which are then detected by capillary electrophoresis. The cDNA can be used to determine the identity of the nucleotides on which the adducts have formed more prevalently, designating those areas as single stranded, or unconstrained regions.

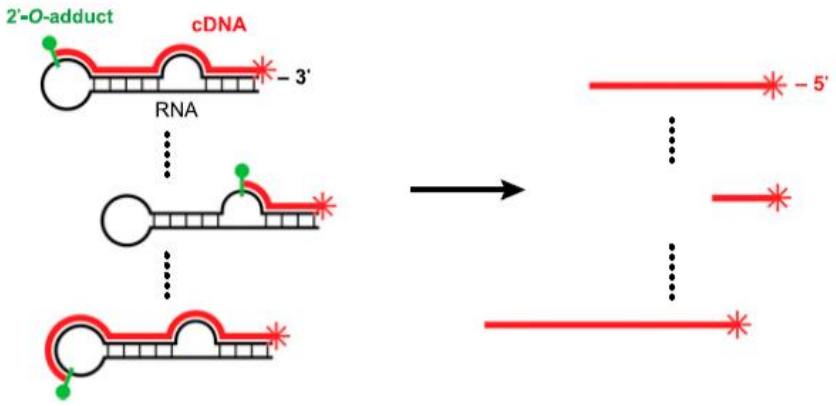

Figure 10. Primer Extension. The schematic above represents the primer extension reactions. 2'-esterification adducts are represented in this figure by the green bulbs. The red lines are the resultant cDNA from the reverse transcription reaction.[25]

Production of cDNA transitions to the last process of hSHAPE chemistry which is the capillary electrophoresis and data analysis. As mentioned above, the resultant cDNA from the reverse transcription reactions are run through capillary electrophoresis. The subsequent electropherogram yields quantitative values reflecting the population of the fluorescently labeled cDNA molecules of various lengths. These quantitative values then indicate the positions of single-strandedness, or high flexibility of each nucleotide in the RNA.

After the electropherogram has been generated, it is run through ShapeFinder software for data analysis. Here, the program takes the generated data from a positive control experiment (incudes the nucleophile) and subtracts a negative control experiment (without the nucleophile) to remove any background and produces the raw data. It is this data that contains the hSHAPE reactivity values for each nucleotide in the RNA sequence.[26]

These values are then transferred to an additional software program, RNAstructure, for predicted RNA folding. It is with this program that the two dimensional RNA secondary

structure is generated using free energy, nearest-neighbor parameters. With the inclusion of the pseudo-energy constraints provided by the SHAPE reactivity data from ShapeFinder, the RNAstructure program can fold the RNA with improved structure prediction accuracy.[27]

The utilization of the three techniques previously described, allowed us to do the following: The EMSA gels allowed us to observe the formation of the IRP-IRE complex under uninhibited and metal ion conditions, the AFM experiment provided us with a physical representation of the formation of the IRP-IRE complex, and lastly, the hSHAPE chemistry experiments provided intricate two dimensional IRE RNA modeling under various conditions, such as bound with the IRP and interference by metal ions.

CHAPTER 2

EXPERIMENTAL METHODS

2.1 DNA Synthesis

A polymerase chain reaction (PCR) was used to amplify 132 base pair and 77 base pair FTH1 IRE RNAs. The DNA was synthesized with a forward primer, bearing a T7 promoter sequence, a reverse primer, and a 75nt cassette template, all purchased from Integrated DNA Technologies, Inc (IDT). The sequences are shown in Table 1 below. The PCR mixture (500 µL total volume) used to synthesize the DNA contained the following: 20 mM Tris (pH 8.4), 50 mM KCl, 2.5 mM $MgCl_2$, 0.2 mM of each dNTP (dATP, dGTP, dCTP, and dTTP), 0.5 µM each of forward and reverse primer, 0.1 nM of DNA template, and 0.025 units/µl Taq DNA polymerase. The PCR reactions were run using an Eppendorf Mastercycler® personal Authorized Thermal Cycler. The following PCR conditions were used: Denaturation at 94°C for 45 seconds, Annealing at 65°C for 30 seconds, and Extension at 72°C for 30 seconds all repeated for 36 cycles followed by a 15 minute period at 72°C following the 36^{th} cycle. The resultant DNA PCR product was run on a 1.5% agarose gel electrophoresis system from BioRad Laboratories, Inc. for 30 minutes at 120 volts, and the gel was imaged using ethidium bromide staining techniques (Figure 11). The product was then purified via ethanol precipitation and quantified using the General Electric Heathcare, NanoVue UV/Vis spectrophotometer.

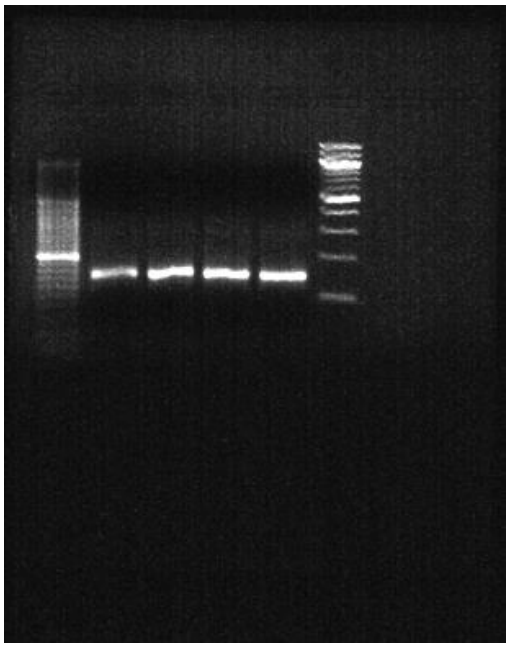

Figure 11. DNA PCR Product. Image of ethidium bromide stained 1.5% agarose gel used to determine quality of DNA PCR product. A 20 base pair and 200 base pair ladder were used.

Table 1. Sequences of DNA PCR Reactions. The forward and reverse primers, and template used for DNA PCR reactions.

FTH1 IRE Forward Primer	5'TAATACGACTCACTATAGGCCTTCGGGCCAAGTTCTTCGCCGA GAGT 3'
FTH1 IRE Reverse Primer	5'GAACCGGACCGAAGCCCGATTTGGATCCGGCGAACCGGATCG AGGGGTGGGGACGAGCG 3'
FTH1 IRE 75nt Template	5'GTTCTTCGCCGAGAGTCGTCGGGGTTTCCTGCTTCAACAGTGCT TGGACGGAACCCGGCGCTCGTTCCCCACCCC 3'

2.2 RNA Synthesis

The 77nt and 132nt RNA were transcribed in a 1mL reaction using 50ug of DNA from the IRE PCR reactions. The transcription solution also contained 40 mM Tris (pH 7.8), 20 mM NaCl, 6 mM $MgCl_2$, 2 mM spermindine HCl, 10 mM DTT, 1 mM of each NTP (ATP, GTP, CTP, and UTP), 0.1 units/µl SUPERaseIn^{TM}RNase inhibitor, and two units/µl T7 RNA polymerase. This transcription reaction was incubated for a period of three to four hours at 37°C.

After transcription, DNA template degradation was completed using two units/µL of TURBO™ DNase in a 15 minute reaction at 37°C. The DNase was then deactivated using 0.5M EDTA and heating the solution to 75°C for ten minutes. After DNA template degradation, the RNA was purified by ethanol precipitation. Further purification of the 77 and 132nt IREs to be used for AFM and hSHAPE chemistry respectively was done using an 8% denaturing polyacrylamide gel electrophoresis (PAGE) experiment run at 12 watts for ~1.5 hours. The RNA was detected under UV illumination, and the bands we cut out by hand for passive elution. Theses gel strips containing the RNA were eluted for a period of 12 hours, on rotary, at 4°C in 1 mL of a 0.5 mM sodium acetate, 1 mM EDTA solution. The resultant eluate was ethanol precipitated to concentrate the RNA, which was then quantified using the NanoVue UV/Vis spectrophotometer. 52nt IRE RNA was also used for some comparative experiments, however this was directly purchased from IDT.

2.3 IRP Synthesis

In initial studies, the IRP protein was purchased from OriGene Technologies, Inc. for use in our experiments. However upon receiving the protein multiple times in the ACO-1 conformation and not the IRP conformation, we began our own protein over-expression and purification to generate the IRP following the protocol from OriGene.

2.3.1 Plasmid Cloning and Purification

ACO-1 plasmid was cloned by transforming XL1-Blue Competent E. coli cells (Agilent Technologies # 200249) with ACO1 (Myc-DDK-tagged)-Human aconitase 1 ORF plasmid (OriGene # RC201857). Transformed XL1-Blue cells were grown in LB media containing 50 µg/ml Kanamycin for 16 hours. Plasmid was then purified using a QIAGEN Plasmid Maxi Kit

(QIAGEN # 12162) and re-suspended in T.E buffer pH 8.0 (10 mM Tris, pH 8.0; 1 mM EDTA, pH 8.0).

2.3.2 Protein Over-Expression and Purification

The protein over-expression and purification protocol was developed by Andrea Belalcazar with the guidance of OriGene tehnical support. 293T/17 Human Embryonic Kidney cells (ATCC # CRL-11268) were grown in DMEM Medium (high glucose with sodium pyruvate and L-glutamine) (Fisher # SH30243FS) containing 10% FBS. When cells reached 70-80% confluency, DMEM media was replaced with Opti-MEM I Reduced Serum Medium (Life Technologies # 11058-021). The cells were then transfected with the cloned ACO-1 plasmid using TurboFectin Transfection Reagent (Ori-Gene # TF81005).

After four days of transfection, cells were washed with PBS and lysed with CelLytic M lysis buffer (Sigma # C2978-250ML) containing a Protease Inhibitor Cocktail (Sigma # P8340-5ML). ACO-1 protein was purified from the lysate using ANTI-FLAG M2 Affinity Gel (Sigma # A2220) in SigmaPrep spin columns (Sigma # SC1000-1KT). The unwanted proteins were washed from the columns with PBS. The Protein was then eluted with 0.1 M glycine, pH 3.5. The pH of the solution was then made less acidic with the addition of 25 µl/ml Tris-HCl, pH 8.0. The protein was then concentrated using Amicon Ultra Centrifugal Filters (Millipore # UFC203024). The purified protein was then stored in this buffer at -80°C until needed for experiments.

2.4 EMSA Experiments

2.4.1 IRE Comparative Gel

The first EMSA experiments compare the 52nt IRE (5'-AGAGU CGUCG GGGUU UCCUG CUUCA ACAGU GCUUG GACGG AACCC GGCGC UC-3'), the 77nt IRE (5'-GGCCU UCGGG CCAAG UUCUU CGCCG AGAGU CGUCG GGGUU UCCUG CUUCA ACAGU GCUUG GACGG AACCC GGCGC UC-3') used in AFM experiments, and the 132nt IRE (5'- GGCCU UCGGG CCAAG UUCUU CGCCG AGAGU CGUCG GGGUU UCCUG CUUCA ACAGU GCUUG GACGG AACCC GGCGC UCGUU CCCCA CCCCU CGAUC CGGUU CGCCG GAUCC AAAUC GGGCU UCGGU UCCCG UUC-3') used in hSHAPE chemistry experiments. It was conducted to demonstrate both purity of each IRE RNA, and binding ability to IRP. The ratio of IRP to IRE in this experiment was kept at 10:1, IRP:IRE. The EMSA had separate 10 µL reaction solutions with and without the IRP containing the following: 0.2 µM of each respective IRE, 2 µM of IRP, 2.5X Binding Buffer (40 mM HEPES (pH 7.3), 80 mM KCl, 4 mM $MgCl_2$, 4 mM DTT, and 20% Glycerol), and nuclease free H_2O. The solutions containing IRE and IRP underwent a 15 minute incubation period at room temperature to allow for IRP-IRE complex formation. Each reaction was run in separate wells on an eight-well (7 cm x 7 cm), 2% agarose gel at 120 volts for 30 minutes on a BioRad gel electrophoresis system submerged in a 1X TBE buffer. The resulting gel was then stained for 30 minutes using Lonza SYBR Green II RNA staining and then imaged under UV fluorescence. The gel was also stained afterwards using Sigma Aldrich EZBlue protein staining mix.

2.4.2 Metal Ion Titration Gel

Metal Ion Titration using Mn^{2+} was conducted to observe the ability of the complex to dissociate under various concentrations of Mn^{2+}. A 16-well (14 cm(W) x 8 cm(L)) gel and C.B.S Scientific Company, Inc. gel electrophoresis apparatus were used for this experiment. Sixteen solutions were prepared for the Mn^{2+} titration. The first three solutions contained IRP only, IRE only, and the IRP-IRE control with no Mn^{2+}. The last 13 solutions contained Mn^{2+} concentrations ranging from 50 µM to 50 mM. Each solution contained a constant 10:1 ratio of IRP:IRE. The 10 µL solution compositions were as follows: 0.2 µM 132nt IRE, 2 µM IRP, (*X)*µM $MnCl_2$, 2.5X Binding Buffer, and nuclease free H_2O. The IRE and IRP underwent a 15 minute incubation period to allow for complex formation. The incubation period was then followed by an introduction of the $MnCl_2$ at each concentration for each respective solution and a 15 minute interference/interaction period was allowed. The above reactions were performed at room temperature. Afterwards, the solutions were loaded in the gel immersed in a 1X TBE buffer and run for 30 minutes at 120 volts. The gel was then stained for 30 minutes in SYBR Green II and imaged, followed by an EZBlue protein staining. The SYBR Green II image was then analyzed using ImageJ software to determine the intensities of the RNA bands for curve fitting analysis. Upon getting the intensities of each band, the following equation was used to determine fraction of RNA bound:

Equation 1: Fraction bound = $$\frac{bound\ RNA\ intensity}{(bound\ RNA\ intesity + undbound\ RNA\ intesity)}$$

These values were then taken and plotted with the software program Kaleidagraph, generating a graph of fraction bound vs. [Mn^{2+}]. These points were then fit to a logarithmic

equation and a best-fit line was plotted using the software's general curve fit definition option and inserting the following equation:

Equation 2: y= 1-(m2*((m0)/(m0+m1))+m3);m1=1;m2=0.8;m3=0.01

Where m0 represents $[Mn^{2+}]$; m1 represents the transition midpoint, $[Mn^{2+}]_{1/2}$; m2 represents the transition amplitude; m3 represents the small baseline offset.

The resulting best-fit line was then calculated and plotted along the points of the generated graph.

2.4.3 Mn^{2+} Pre-Incubation Experiments

For this set of EMSA experiments the period in which the Mn^{2+} ions were introduced to our complex was changed. The Mn^{2+} ions were introduced to the IRE and IRP independently prior to complex formation. We introduced 500 µM $MnCl_2$ to IRE and IRP solutions for 15 minutes at room temperature prior to binding. In some of these experiments, either the IRE or the IRP was incubated individually in 500 µM Mn^{2+} and the other member of the binding pair was not exposed to Mn^{2+} in order to investigate the effects on each binding partner. We then combined each component in a 10 µL mixture for complex binding. The experiments we ran were either a protein titration (IRP:IRE ratios of 20:1, 10:1, 5:1, 2:1, and 1:1) or a constant 3:1 IRP:IRE ratio with different Mn^{2+} incubation conditions. The mixture again contained 500 µM $MnCl_2$, 0.2 µM IRE RNA previously incubated in Mn^{2+}, 0.6 µM IRP (3:1 experiment) previously incubated in Mn^{2+}, 2.5X Binding buffer, and nuclease free H_2O. The complex formation incubation period was again 15 minutes at room temperature followed by electrophoresis in a 1X TBE buffer at 120 volts for 30 minutes on the eight-well BioRad

electrophoresis apparatus. The experiment was also concluded with a SYBR Green II RNA staining and an EZBlue Protein staining.

2.5 hSHAPE Chemistry Experiments

As mentioned in the introduction, hSHAPE chemistry is the acronym for a process. The steps in the hSHAPE chemistry process are sequentially described in detail here.

2.5.1 Selective 2' Hydroxyl Acylation

One micro molar 132nt IRE in a 0.5X TE buffer was heated at 95°C for two minutes and then placed on ice for two minutes for proper conformational folding of the RNA. The IRE to be used for the sequencing (ddNTP) reaction was kept on ice for the duration of the acylation reactions. The IRE undergoing acylation was then mixed with the 2.5x Binding Buffer and placed at 37°C for 20 minutes. After this 20 minute incubation, depending on the experiment, IRP and/or $MnCl_2$ was added after this step. IRP and IRE were incubated together for 15 minutes followed by a 15 minute incubation in the experiment's desired $MnCl_2$ concentration, all at room temperature. When IRP was involved, 2 µM concentrations were used to keep the ratio of IRP:IRE at 10:1. After this step, 2'hydroxyl adduct formation was initiated. The solutions were split into two tubes for a (+) reaction with the nucleophile 1-methyl-7-nitroisatoic anhaydride (1M7), and a (-) reaction, without the 1M7. 1M7 diluted in dimethyl sulfoxide (DMSO) was added to the (+) reaction at a final concentration of 3 mM for adduct formation. Only DMSO was added to the (-) reaction. These solutions were then incubated for two minutes at 37°C followed by an ethanol precipitation to obtain and concentrate the IRE with formed adducts.

2.5.2 Primer Extension

The primer extension reactions included the (+) reaction, (-) reaction, and a sequencing reaction. Different fluorescently labeled DNA primers (5'-GAACCGGACCGAAGCCCG-3') were added to each of the three reactions. The reactions were incubated at 65°C for six minutes followed by a 15 minute incubation at 35°C. Afterward, a reverse transcription buffer (50 mM Tris-HCL (pH 8.3), 75 mM KCL, 3 mM $MgCl_2$, 5 mM DTT, 0.5 mM dATP, dGTP, dCTP, dTTP, and nuclease free H_2O) was added to each reaction, along with a ddNTP (A,T,C, or G) to only the sequencing reaction. The reactions are then heated to 52°C for one minute. Next, the reverse transcriptase enzyme (SuperScript III, from Life Technologies, Corp.) was added to all reactions and allowed to incubate for an additional ten minutes at 52°C. Afterwards, a sequencing stop mix (1:1 of 100 mM EDTA: 3M NaOAc) was added to each reaction to stop the reverse transcription. The (+) reaction, (-) reaction, and sequencing reaction were combined to a single tube and ethanol precipitated to collected the newly formed cDNA fragments.

2.5.3 Capillary Electrophoresis

cDNA fragments are separated by size via capillary electrophoresis. Capillary electrophoresis experiments were done on an ABI Prism® 310 Genetic Analyzer (Figure 12) from Applied Biosystems. The genetic analyzer was cleaned and pre-loaded with a 1X ABI buffer and Performance Optimized Polymer 4 (POP-4™) prior to use. Each run consisted of one combination of reactions. Runs lasted for 25 minutes and were kept at 15kV and 60°C. After runs were completed, the raw electropherogram data was stored to the computer hard drive to be used for analysis.

Figure 12. ABI 310 Genetic Analyzer. This was used to conduct capillary electrophoresis experiments during hSHAPE chemistry.

2.5.4 Data Analysis

Upon completion of a run, electropherogram data was transferred to a computer containing ShapeFinder software. This software was used to obtain the annotated shape values for each nucleotide in the sequence. The data underwent baseline adjustments, matrixing, and mobility shift adjustments. Next, peaks for the (+) and (-) control data were manually aligned by the user and then the software integrated the (+) and (-) peaks, providing normalized data for each nucleotide in the sequence. The normalized data was then transferred to another computer with RNAstructure software developed by Matthews Laboratories for secondary structure predictions. This program uses free energy, nearest-neighbor parameters in concert with the normalized SHAPE data as a pseudo-energy constraint to accurately predict the secondary structure of our IRE with high accuracy (90-95%).[23] The program then generated a series of predicted secondary structures beginning with the lowest energy structure conformation.

2.6 AFM Experiments

To conduct the AFM experiments, a construct needed to be developed to image the IRP-IRE complex. This construct was derived from a series of SPR experiments that were being conducted by the Day Lab at Marshall University. G3 Dendrons were conjugated with a complimentary 26 base pair NH_2-DNA strand ordered from IDT to act as the base of our construct. Before each AFM experiment, the conjugated dendrons were reacted with hydroxylamine for 30 minutes to expose the thiol groups of the dendron for binding to the gold surfaces. All surfaces used for the experiments were 1mm x 1mm (111) Gold annealed Mica surfaces purchased from the PHASIS group in Switzerland. 500 pM dendron solutions were used to achieve resolution of single molecules and not a monolayer formation. After the hydroxylamine reaction, a 5 µL droplet was applied to the Gold-Mica surface. All dendron-to-surface binding steps were allowed five minutes of interaction to ensure binding. Once the sample surface was ready, the surface was placed in a solution cell in the Bruker Corporation Atomic Force Microscope for solution cell non-contact mode scanning (Figure 13).

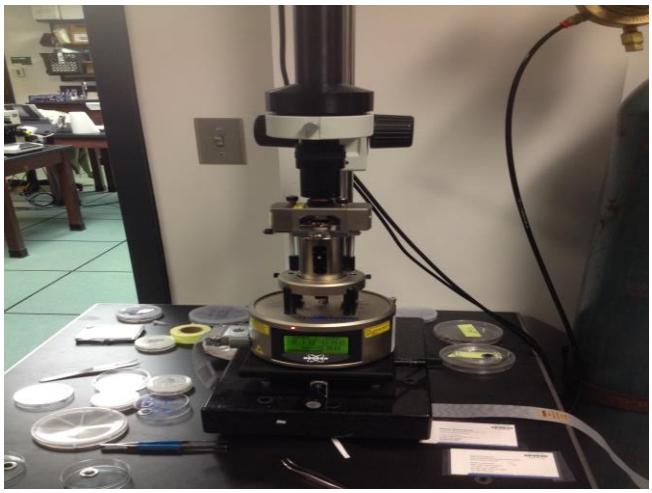

Figure 13. Bruker Corporation Atomic Force Microscope. The microscope is located in the Norton Lab at Marshall University and was used for AFM experimentation.

The solution cell was filled with TE Buffer (pH 8.0) after the surfaces were reacted with the 500 pM dendron solution. Images were then taken to determine z-heights of the dendrons on the surface. Next, 77nt IRE RNA was added to the surface for a total IRE concentration of 10 nM and allowed 15 minutes for binding to the complementary DNA dendrons (5'- TCGGC GAAGA ACTTG GCCCG AAGGCC/3AmMC6T/-3'). The cell was then washed with 1X Binding Buffer (10mM HEPES (7.3 pH), 20 mM KCl, 1 mM $MgCl_2$, 1 mM DTT, 5% Glycerol) and imaged to observe the next stepwise increase in z-height. After the IRE addition scans, 20 nM of IRP was added to the solution cell and allowed 30 minutes to interact for complex formation. Scans were being run during this 30 minute binding period to observe the final increases in z-height of any DNA-IRE-IRP complexes on the Gold-Mica surface. Lastly, 500 µM of $MnCl_2$ was added to the solution cell and imaged over a period of 20 minutes to observe any decreases in z-height, which could be indicative of complex dissociation. The resulting images from all scans were processed using Bruker's NanoScope Analysis software.

CHAPTER 3

EXPERIMENTAL RESULTS

The first set of experiments conducted were done to observe the binding of the IRP-IRE complex using each one of the techniques. Once this was achieved, it was feasible to advance to more interrogative experiments on the complex using any one of the techniques.

3.1 IRP-IRE Complex Formation EMSA Gel Experiment

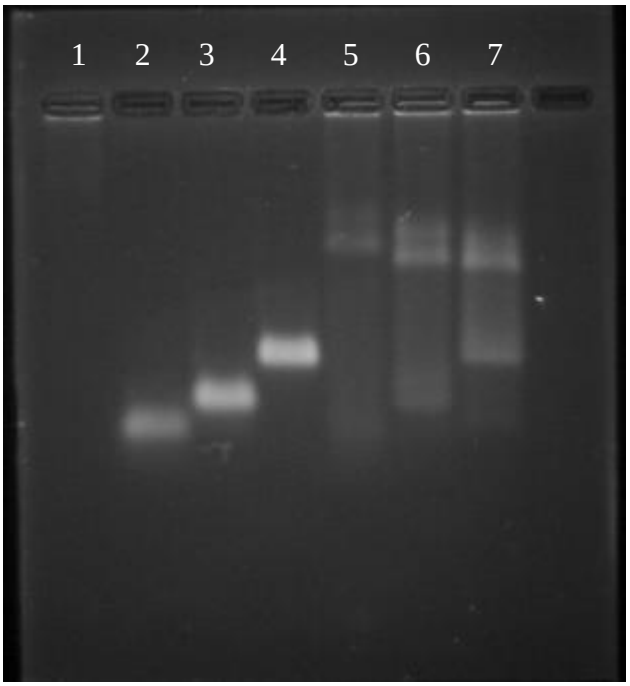

Figure 14. EMSA IRE Comparative Gel. The resultant Gel image comparing 52nt, 77nt, and 132nt IRE RNAs and their complex formation with IRP. Lane 1 is an IRP only lane. Lanes 2-4 are 52nt, 77nt and 132nt IRE only respectively. Lanes 5-7 are the IRE in the same order complexed with the IRP. The concentrations were kept at a 10:1 ratio of IRP:IRE. The six bottom bands represent the migration of free or unbound IRE RNA. The top three bands in lanes 5-7 represent the migration of just the IRP-IRE complex.

3.2 IRP-IRE Complex Formation hSHAPE Chemistry Experiments

After complex formation had been observed using EMSA gels, experiments were run to observe complex formation using hSHAPE Chemistry and to also determine any secondary

structural modifications made to the IRE upon successful complex formation. Additionally, mutant IRE was also used for hSHAPE chemistry experiments. In these experiments, the IRP:IRE ratio was kept at 10:1. Three trials were run on each set of experimental conditions and the figures below represent the averages of each set of experimental conditions.

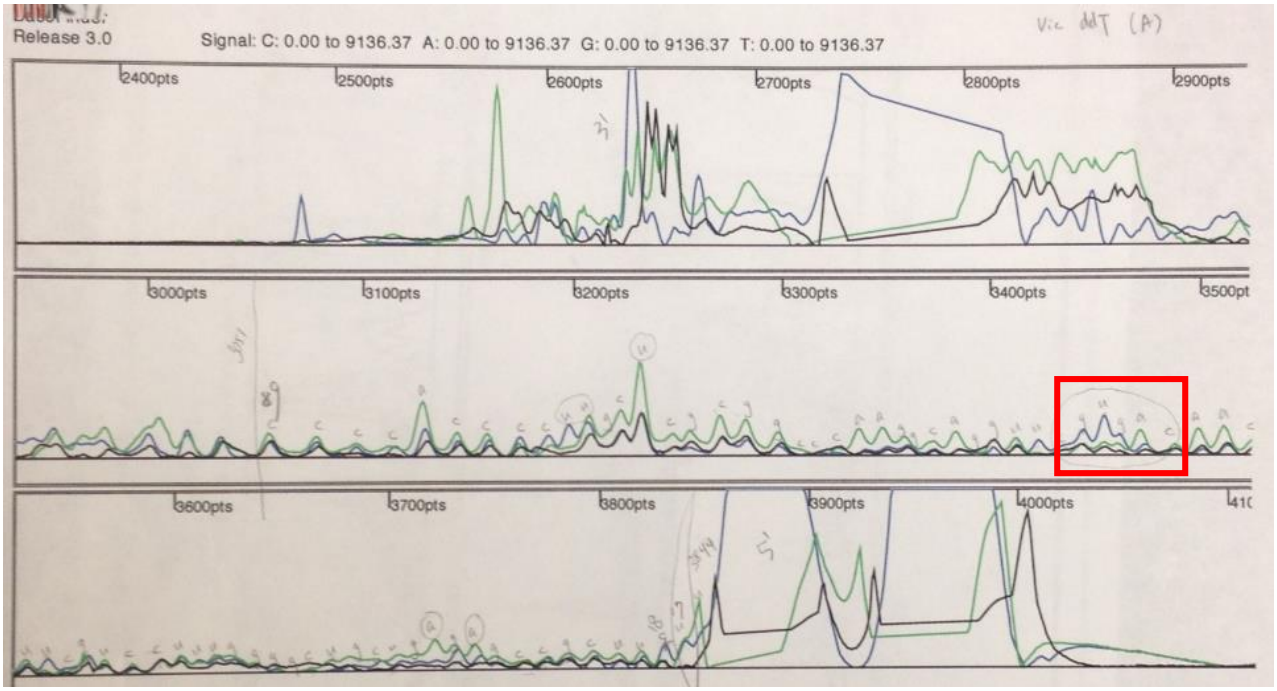

Graph 1. Raw Data Electropherogram of IRE. The data were obtained from the average of three hSHAPE experiments with IRE only in the binding buffer. The highlighted area represents the loop region nucleotides of the IRE where the IRP is known to bind. +1M7 reactions, -1M7 reactions, and ddNTP reactions are represented by the blue, black, and green curves respectively.

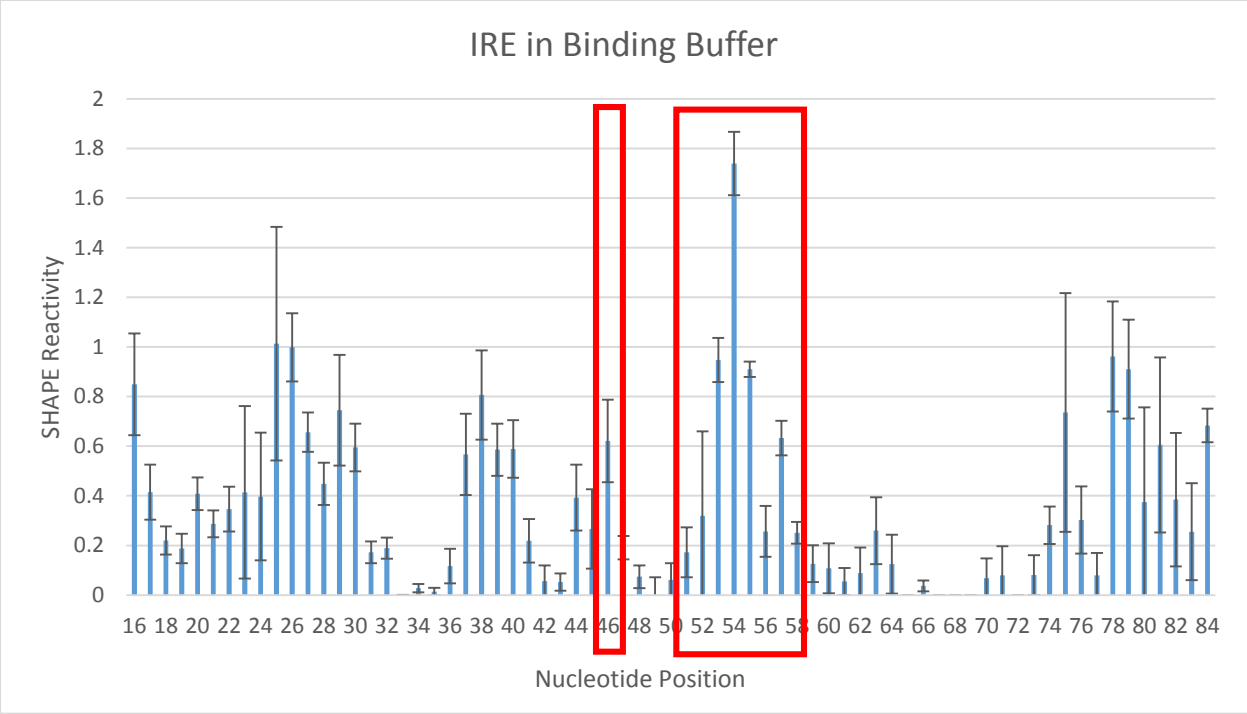

Graph 2. SHAPE Reactivity Histogram of IRE. The histogram is an average of the IRE in binding buffer hSHAPE data. The x-axis represents nucleotide position on the IRE. The highlighted region contains the nucleotides involved in IRP binding. Error bars were derived from standard deviations of the SHAPE reactivity data for each nucleotide.

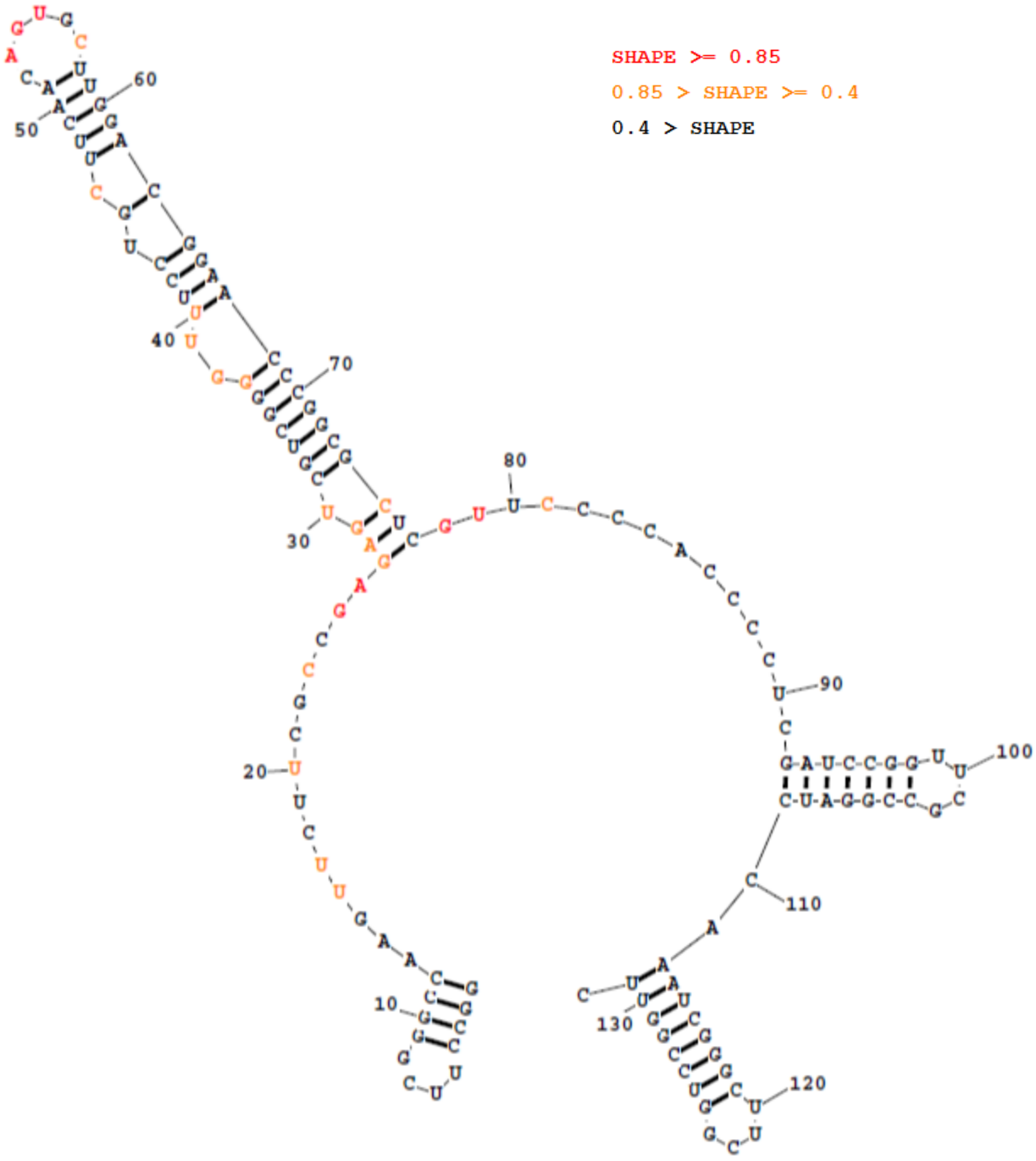

Figure 15. Predicted IRE structure. The secondary structure was folded using RNAstructure software including free energy, nearest-neighbor parameters and the applied SHAPE reactivates for each nucleotide as pseudo-energy constraints. The highlighted loop region is the known area of IRP binding. The annotated shape scale is shown in the upper right corner. It must be noted that ~14nts at the 5' end and ~49nts at the 3' end, although colored black, did not have SHAPE reactivity data.

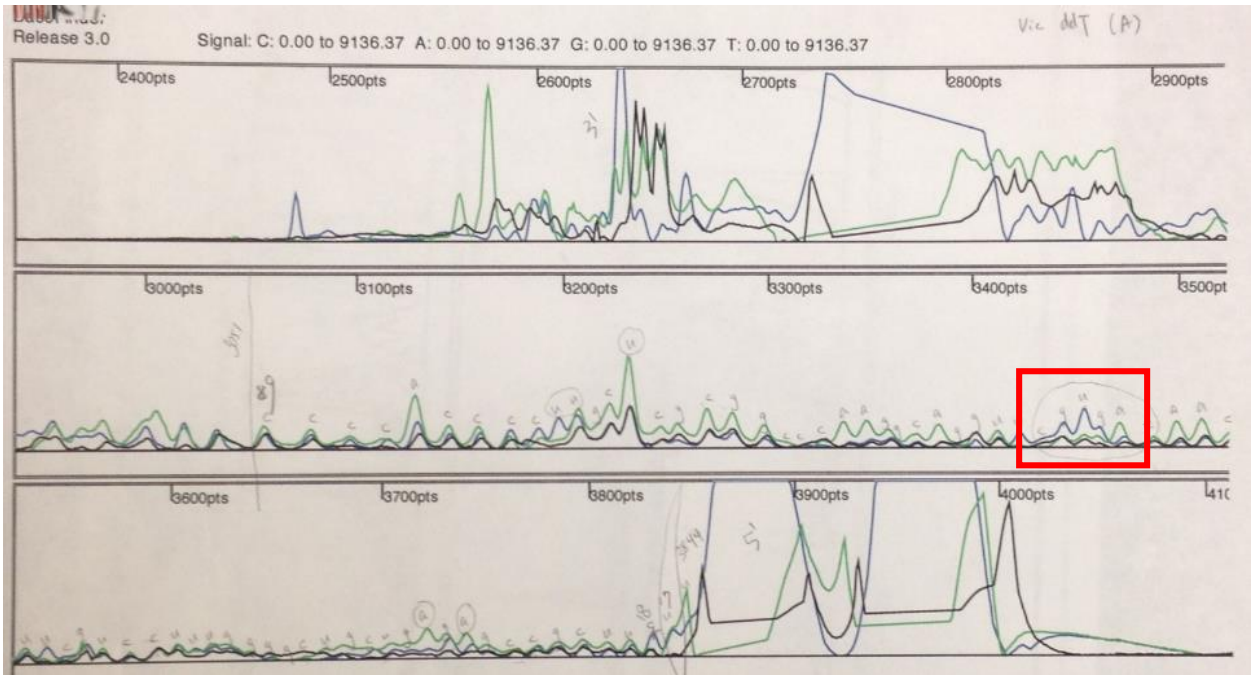

Graph 3. Raw Data Electropherogram of IRE with IRP. The data were obtained from the average of three hSHAPE experiments with IRE bound to the IRP in the binding buffer. The highlighted area represents the loop region nucleotides of the IRE where the IRP is known to bind. +1M7 reactions, -1M7 reactions, and ddNTP reactions are represented by the blue, black, and green curves respectively.

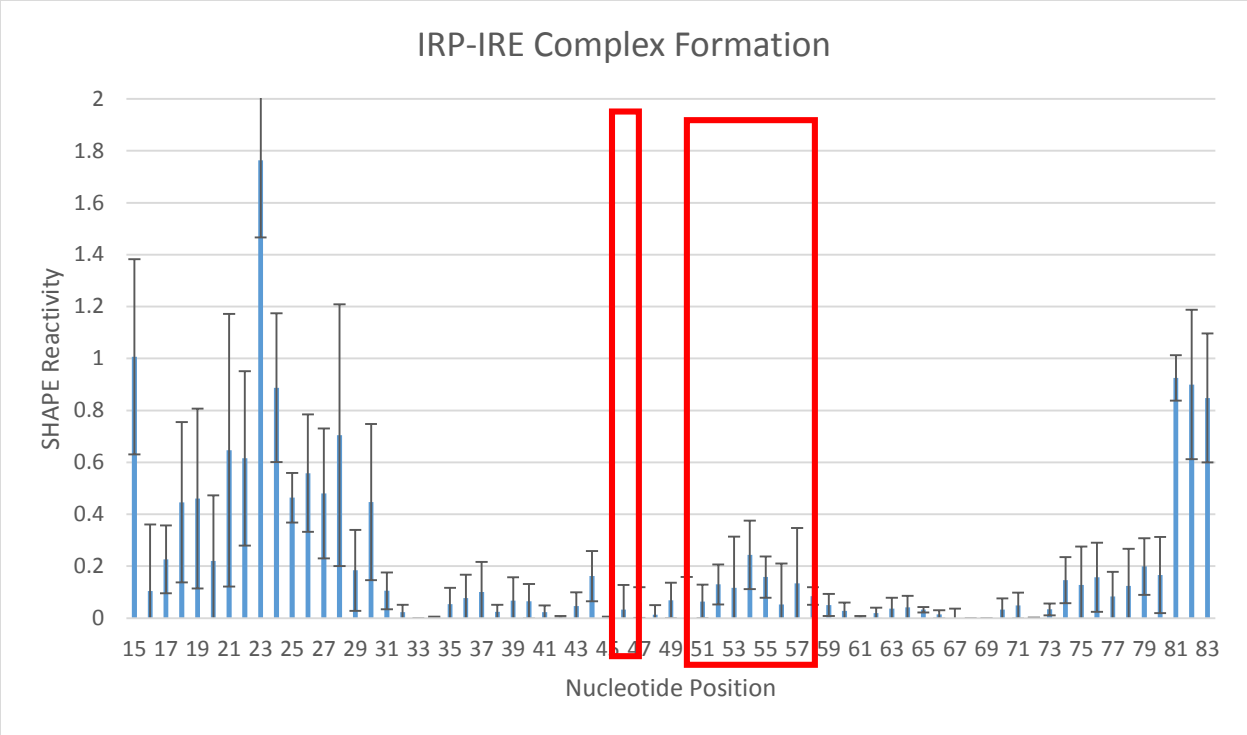

Graph 4. SHAPE Reactivity Histogram of IRE with IRP. The histogram is an average of the IRE SHAPE reactivity data when bound to IRP. The x-axis represents nucleotide position on the IRE. The highlighted region contains the nucleotides involved in IRP binding. Error bars were derived from standard deviations of the SHAPE reactivity data for each nucleotide.

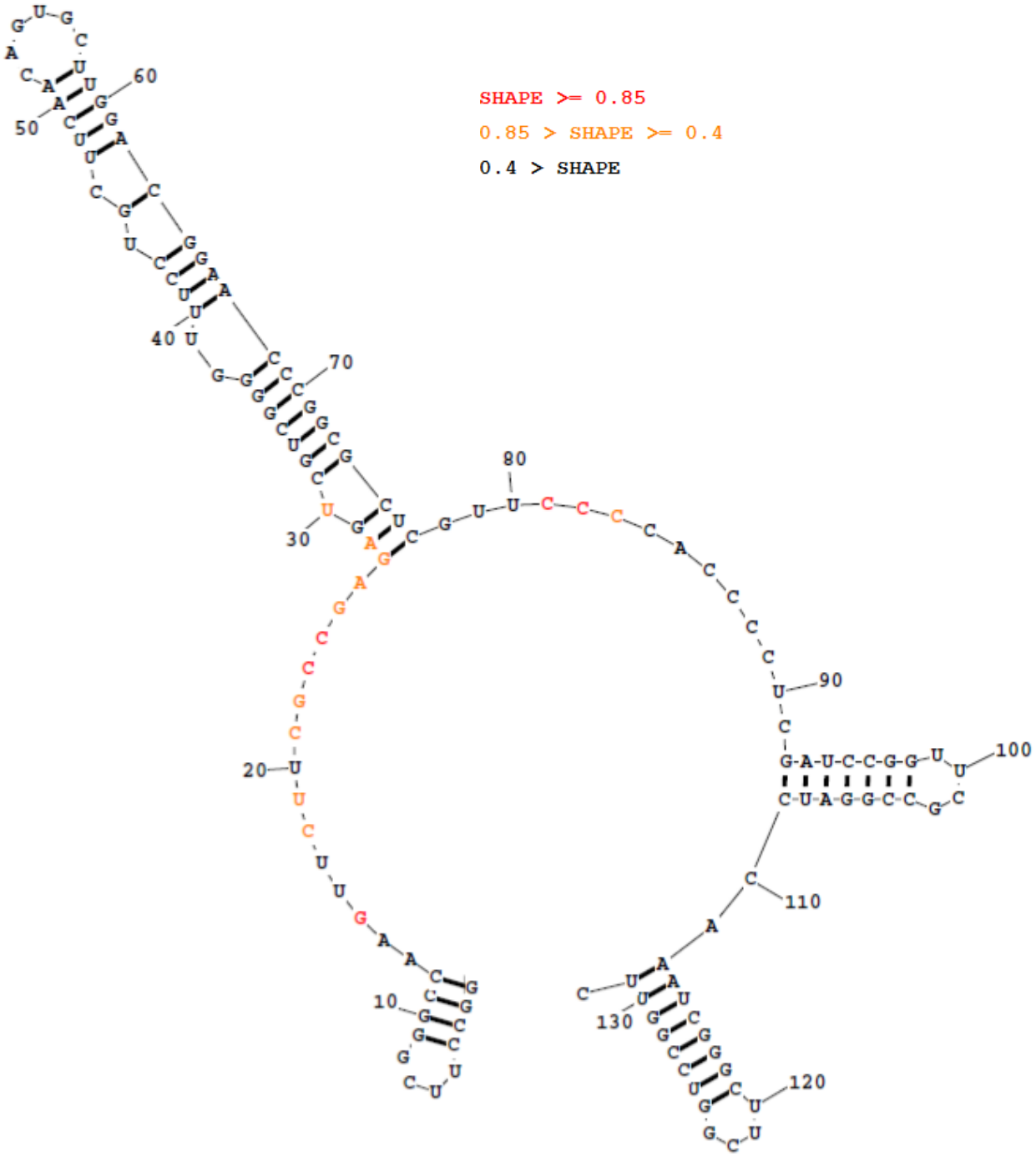

Figure 16. Predicted IRE Structure with IRP. The secondary structure was folded using RNAstructure software including free energy, nearest-neighbor parameters and the applied SHAPE reactivates for each nucleotide as pseudo-energy constraints. The highlighted loop region is the known area of IRP binding. The annotated shape scale is shown in the upper right corner. It must be noted that ~14nts at the 5' end and ~49nts at the 3' end, although colored black, did not have SHAPE reactivity data.

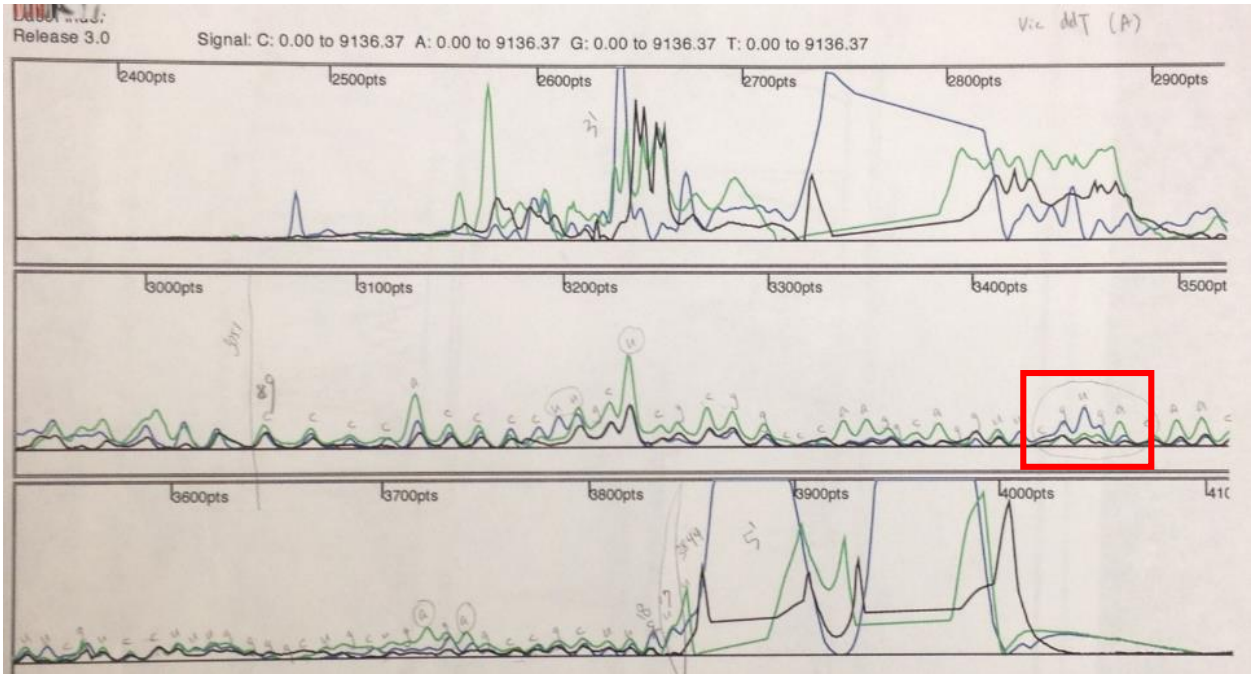

Graph 5. Raw Data Electropherogram of Mutant IRE. The data were obtained from the average of two hSHAPE experiments with mutant IRE in the binding buffer. The highlighted area represents the loop region nucleotides of the mutant IRE where the IRP is known to bind. +1M7 reactions, -1M7 reactions, and ddNTP reactions are represented by the blue, black, and green curves respectively.

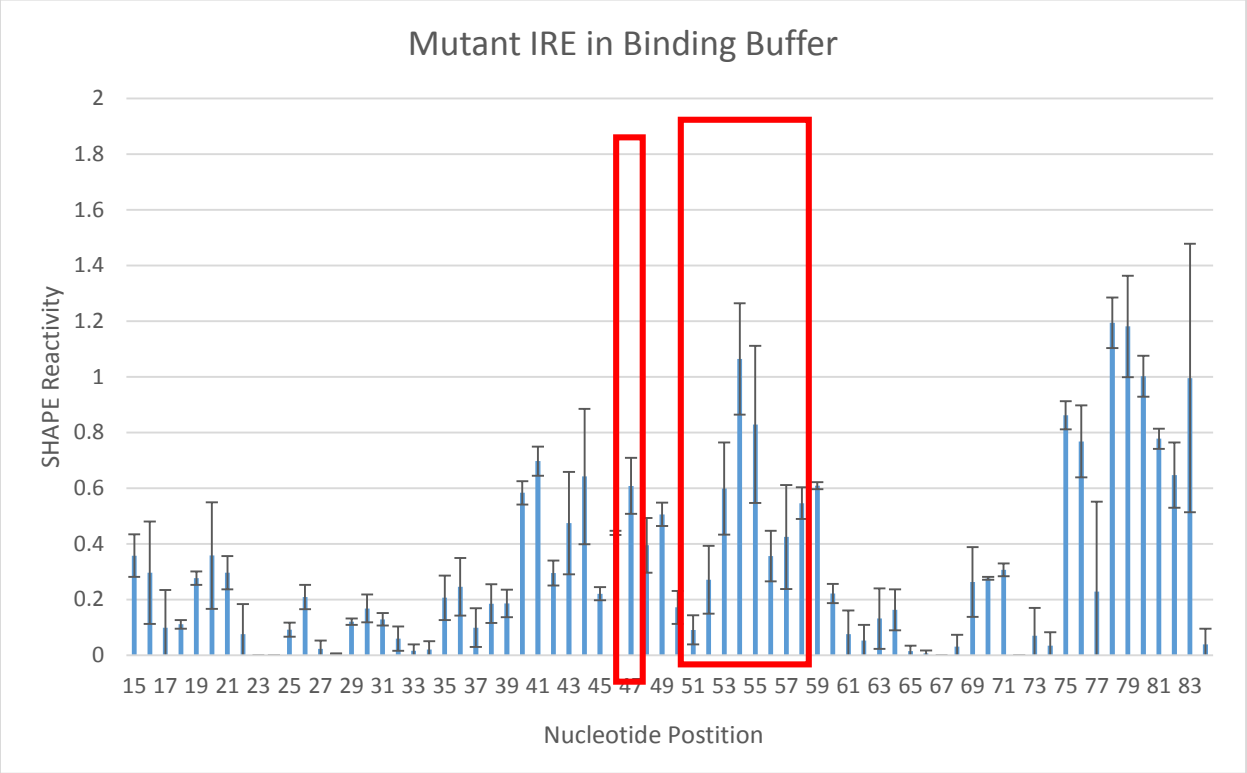

Graph 6. SHAPE Reactivity Histogram of Mutant IRE. The histogram is an average of the mutant IRE SHAPE reactivity data when in the binding buffer. The x-axis represents nucleotide position on the mutant IRE. The highlighted region contains the nucleotides involved in IRP binding. The A→U mutation is located at nucleotide 53. Error bars were derived from standard deviations of the SHAPE reactivity data for each nucleotide.

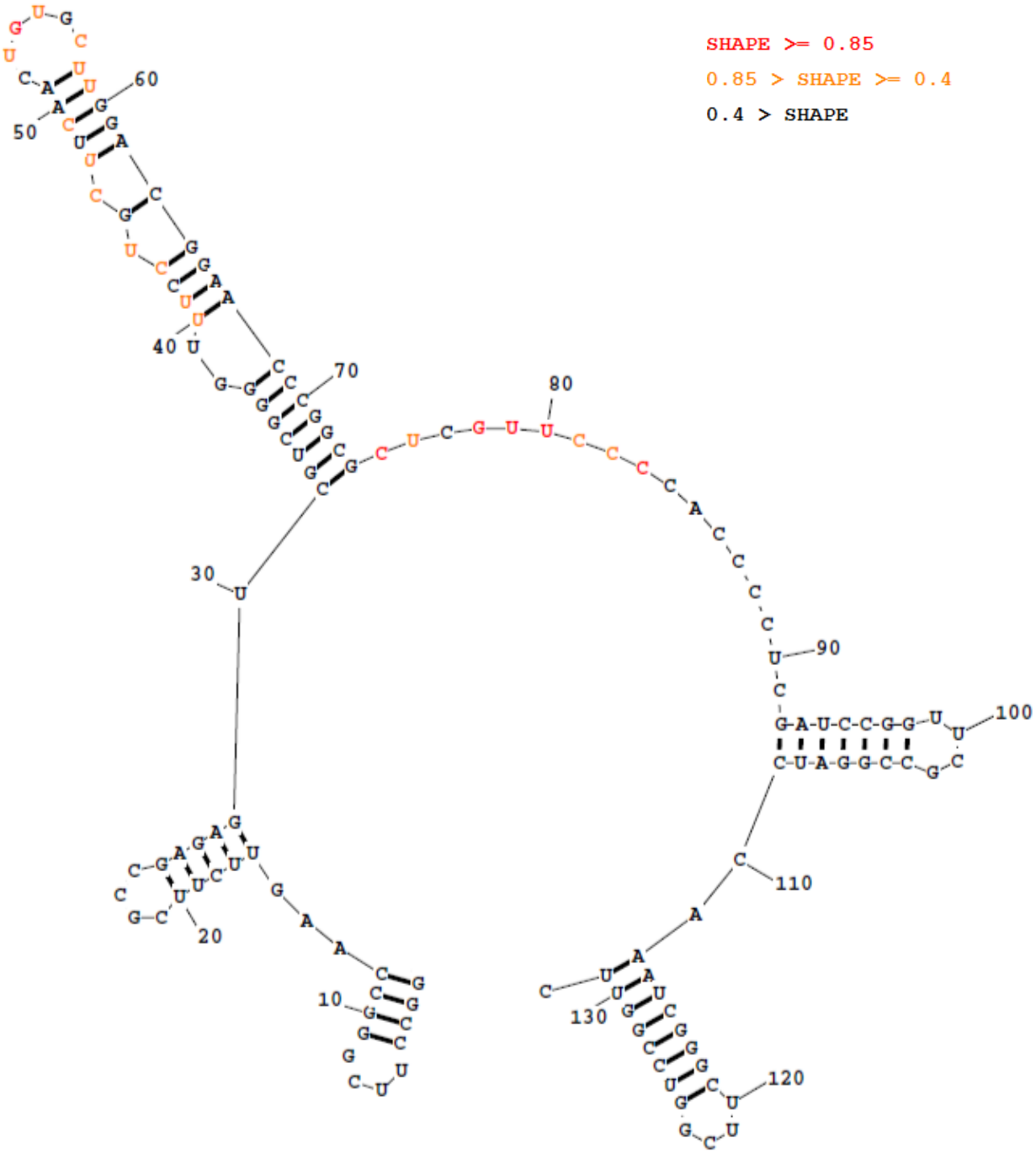

Figure 17. Predicted Mutant IRE Structure. The secondary structure was folded using RNAstructure software including free energy, nearest-neighbor parameters and the applied SHAPE reactivates for each nucleotide as pseudo-energy constraints. The highlighted loop region is the known area of IRP binding. The A→U mutation is located at nucleotide 53. The annotated shape scale is shown in the upper right corner. It must be noted that ~14nts at the 5' end and ~49nts at the 3' end, although colored black, did not have SHAPE reactivity data.

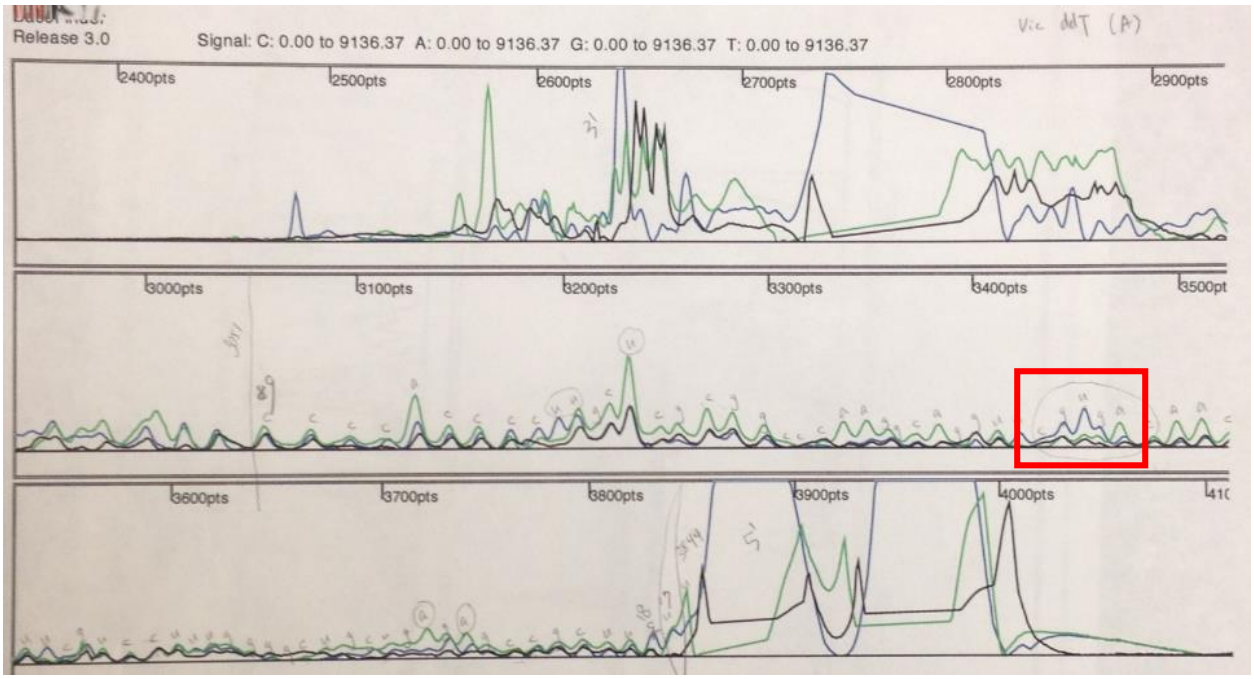

Graph 7. Raw Data Electropherogram of Mutant IRE with IRP. The data were obtained from the average of two hSHAPE experiments with mutant IRE bound to the IRP in binding buffer. The highlighted area represents the loop region nucleotides of the mutant IRE where the IRP is known to bind. +1M7 reactions, -1M7 reactions, and ddNTP reactions are represented by the blue, black, and green curves respectively.

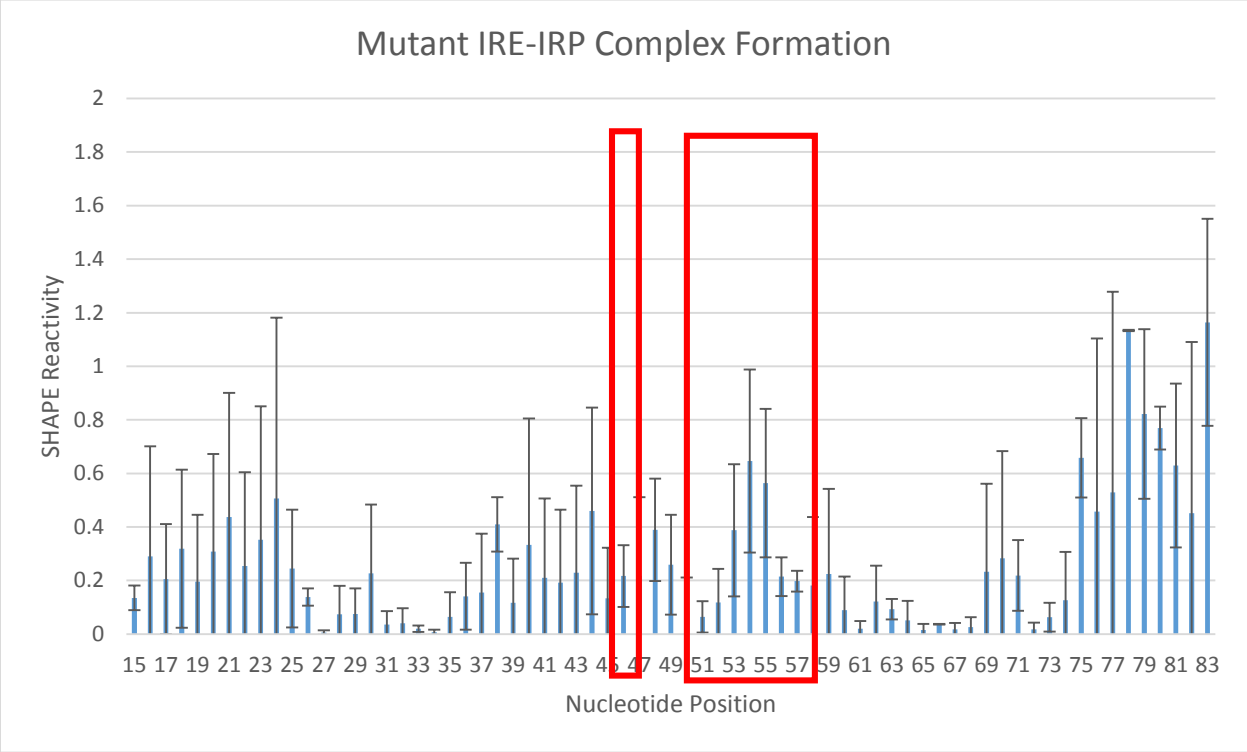

Graph 8. SHAPE Reactivity Histogram of Mutant IRE with IRP. The histogram is the average of the mutant IRE SHAPE reactivity data when bound to the IRP. The x-axis represents nucleotide position on the mutant IRE. The highlighted region contains the nucleotides involved in IRP binding. The A→U mutation is located at nucleotide 53. Error bars were derived from standard deviations of the SHAPE reactivity data for each nucleotide.

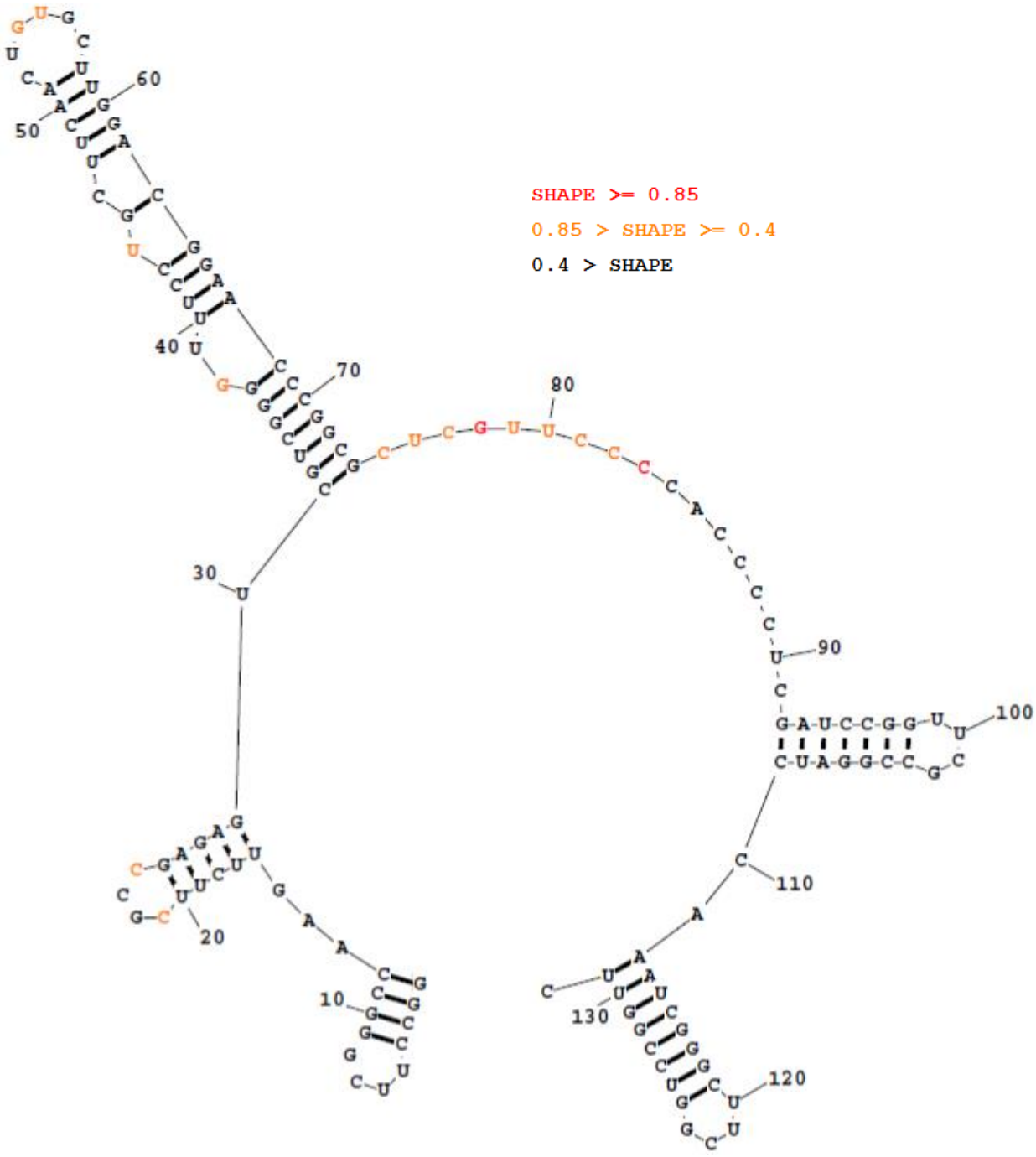

Figure 18. Predicted Mutant IRE Structure with IRP. The secondary structure was folded using RNAstructure software including free energy, nearest-neighbor parameters and the applied SHAPE reactivates for each nucleotide as pseudo-energy constraints. The highlighted loop region is the known area of IRP binding. The A→U mutation is located at nucleotide 53. The annotated shape scale is shown in the upper right corner. It must be noted that ~14nts at the 5' end and ~49nts at the 3' end, although colored black, did not have SHAPE reactivity data.

3.3 IRP-IRE Complex Formation AFM Experiments

Lastly, experiments were conducted using Atomic Force Microscopy to provide a physical representation of complex formation. All resultant images were processes using NanoScope Analysis software. Z-heights of each image were closely observed to determine whether complex formation had occurred on the DNA-IRE-IRP construct.

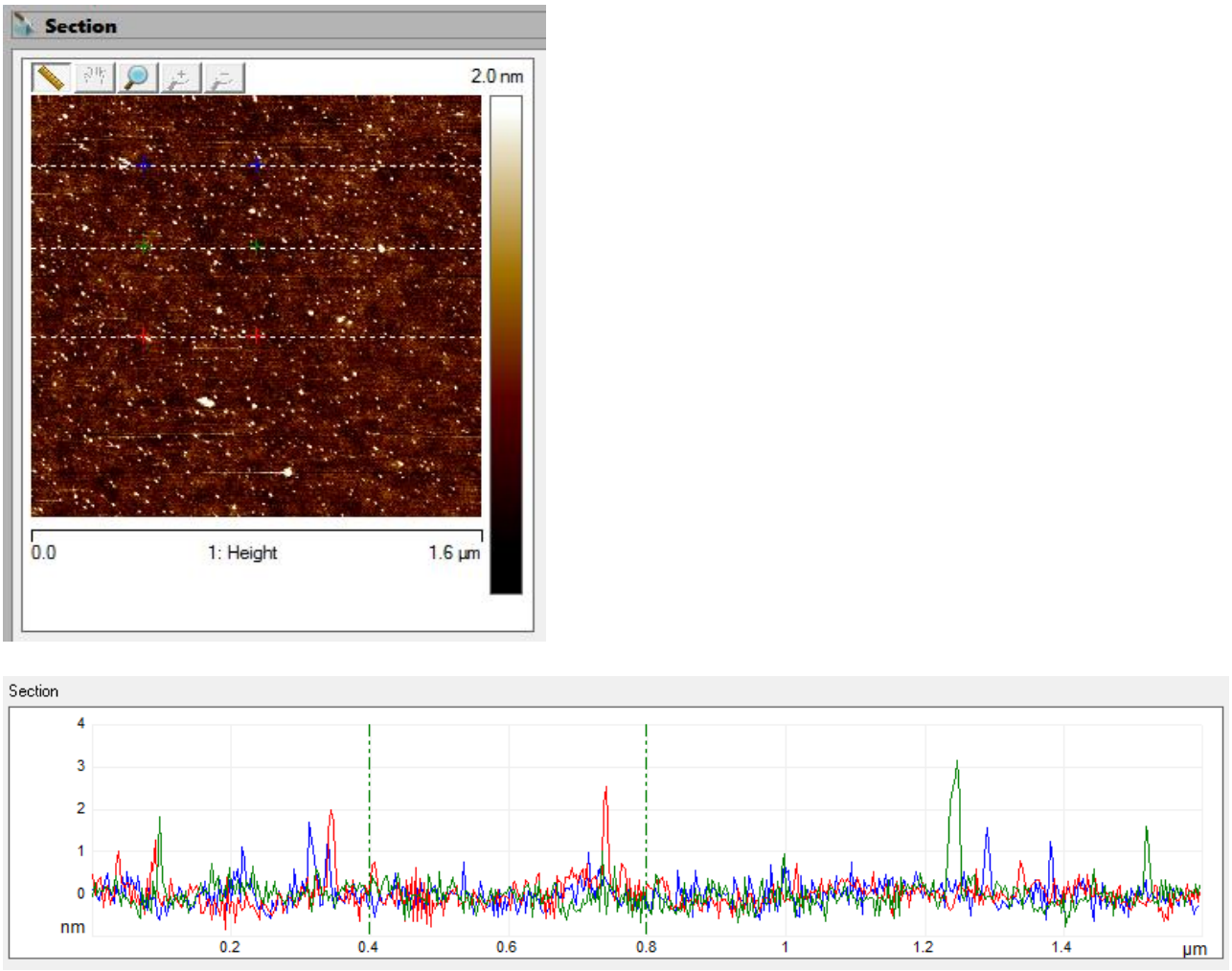

Figure 19. AFM DNA Dendron Image. Displayed is a 1.6 micron AFM scan of only the DNA Dendrons on a gold-mica surface. A line analysis profile from three different lines derived from NanoScope software is shown just below it. It can be seen that the z-height for these dendrons varies between 2-3 nm.

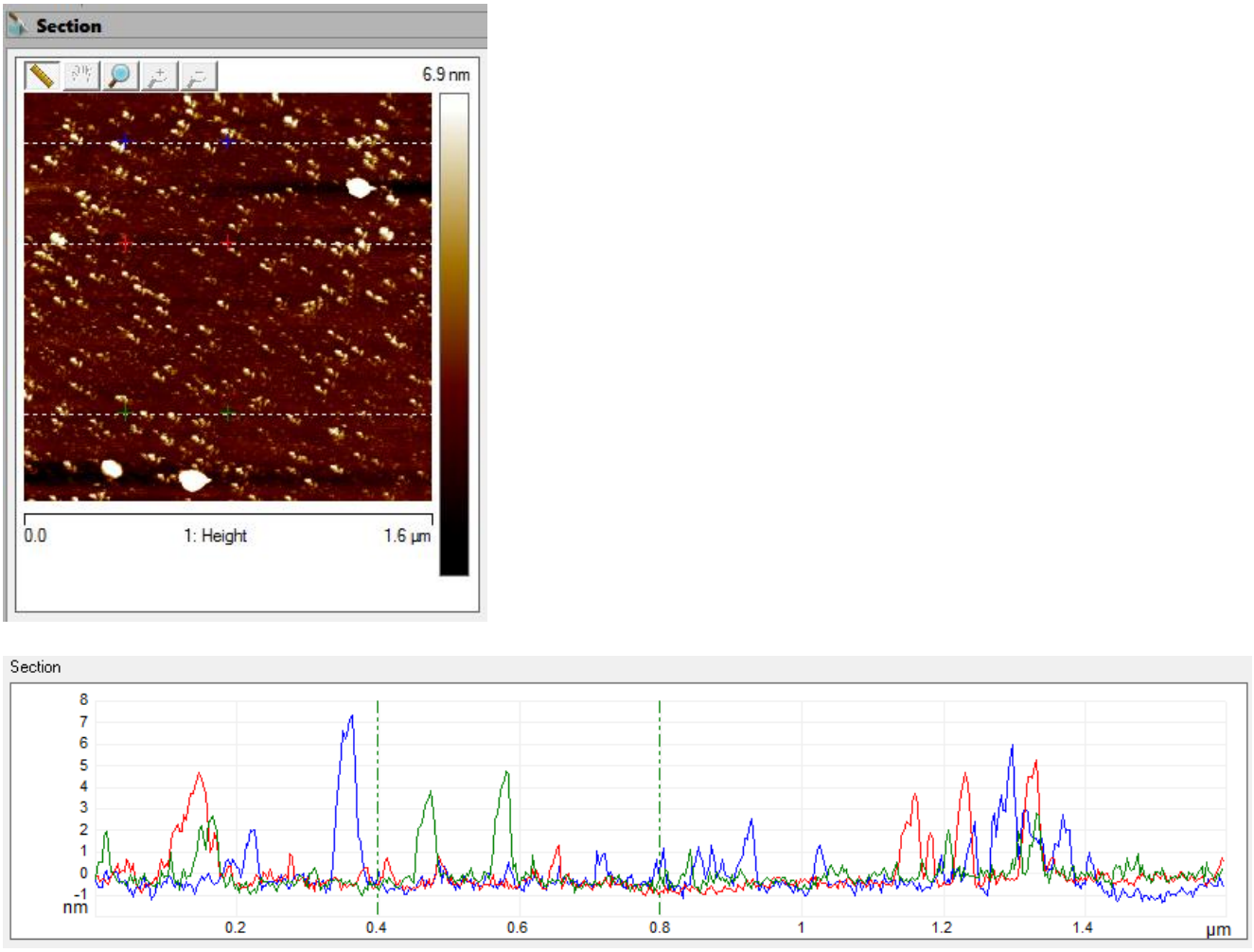

Figure 20. AFM DNA Dendron-IRE-IRP Image. Displayed is a 1.6 micron AFM scan of the DNA Dendron-IRE-IRP all complexed on the gold-mica surface. Once again, line analysis profiles from three different lines derived from NanoScope software are displayed just below it. Now the average height of the features is between 4-6 nm indicating complex formation.

After conducting experiments to observe IRP-IRE complex formation, the next set of experiments was conducted following the Khan group model that Mn^{2+} has the ability to dissociate the IRP-IRE complex once it has formed. EMSA and hSHAPE experiments were run following this model and their results are shown below. AFM experiments were also run using Mn^{2+} to disrupt the IRP-IRE complex; however, the images obtained from these experiments were of poor quality and inconclusive to determine whether the Mn^{2+} was having an effect.

3.4 IRP-IRE Complex Dissociation EMSA Mn^{2+} Titration

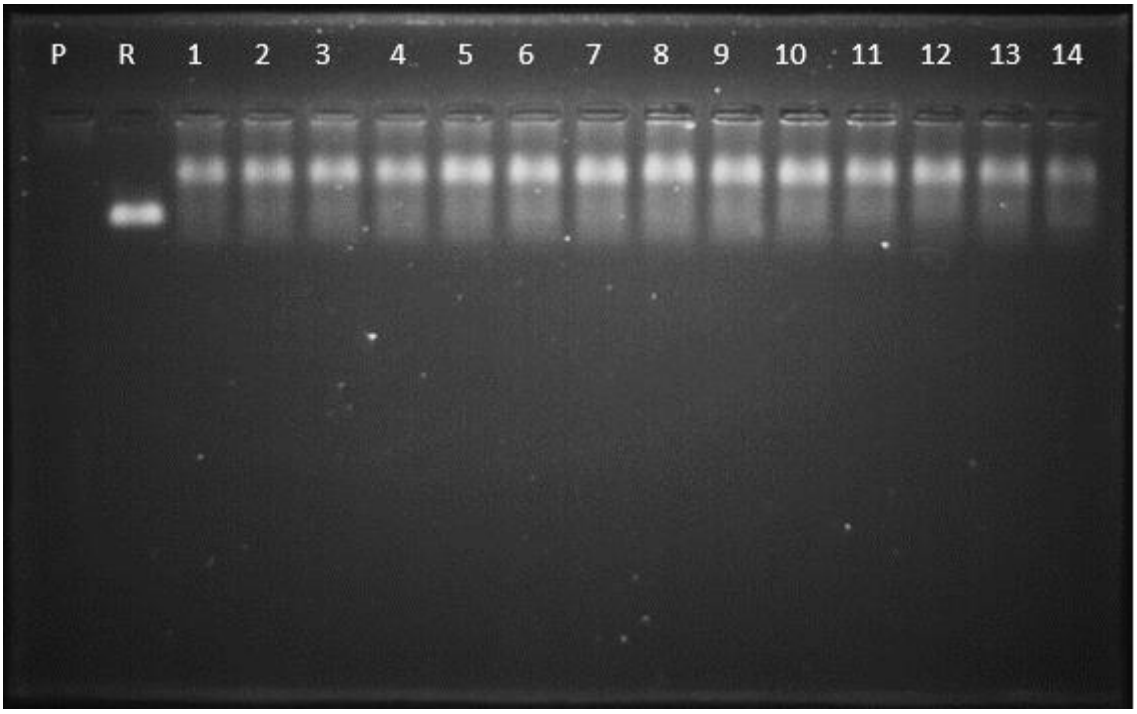

Figure 21. EMSA Mn^{2+} Titration. Above is the resultant SYBR Green II RNA staining of the EMSA Mn^{2+} titration. IRP:IRE concentrations were kept at a constant 10:1 ratio, and only the Mn^{2+} concentrations varied. The top bands represent the IRP-IRE complex. Bottom bands represent the unbound IRE. Lane assignments are as follows: P = Protein only; R= IRE only; 1 = 0µM Mn^{2+}; 2=50µM Mn^{2+}; 3 = 90µM Mn^{2+}; 4 = 150µM Mn^{2+}; 5 = 300µM Mn^{2+}; 6 = 500µM Mn^{2+}; 7=900µM Mn^{2+}; 8 = 1.6mM Mn^{2+}; 9 = 2.8mM Mn^{2+}; 10 = 5.0mM Mn^{2+}; 11 = 9.0mM Mn^{2+}; 12=16mM Mn^{2+}; 13 = 28mM Mn^{2+}; 14 = 50mM Mn^{2+}.

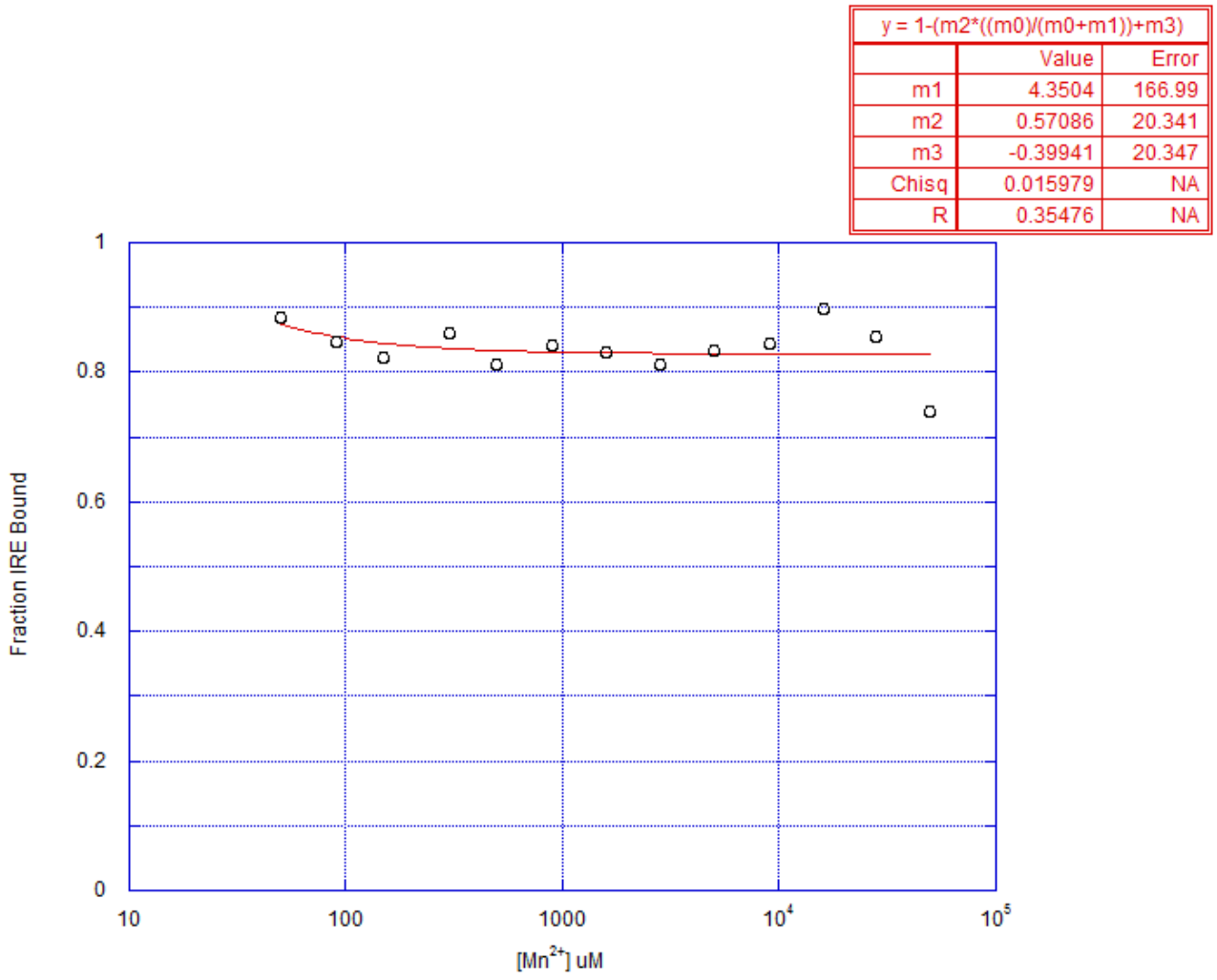

Graph 9. EMSA Mn^{2+} Titration Curve. Above is the graph made from both ImageJ software analysis and Kaleidagraph software analysis. The points on the graph each represent a value of the fraction of the IRE bound as calculated from Equation 1. Values for Equation 1 calculations were provided by ImageJ's gel band intensity function. The curve on the graph was then fit to the points using a logarithmic function as determined by Equation 2 and entered into Kaleidagraph's graphing software. The x-axis represents the concentration of Mn^{2+} and the y-axis represents the fraction of IRE bound. The R^2 value for the best fit line was 35.5.

3.5 IRP-IRE Complex Dissociation by Mn^{2+} hSHAPE Experiments

The experiments conducted to observe complex dissociation by the Mn^{2+} were run on the wild-type IRE only. Concentrations of 50 µM, 500 µM, and 5 mM Mn^{2+} were used to study the complex dissociation in hSHAPE chemistry. All experiments were run at the exact same conditions as the previous IRP-IRE binding experiments with exception of the addition of Mn^{2+}.

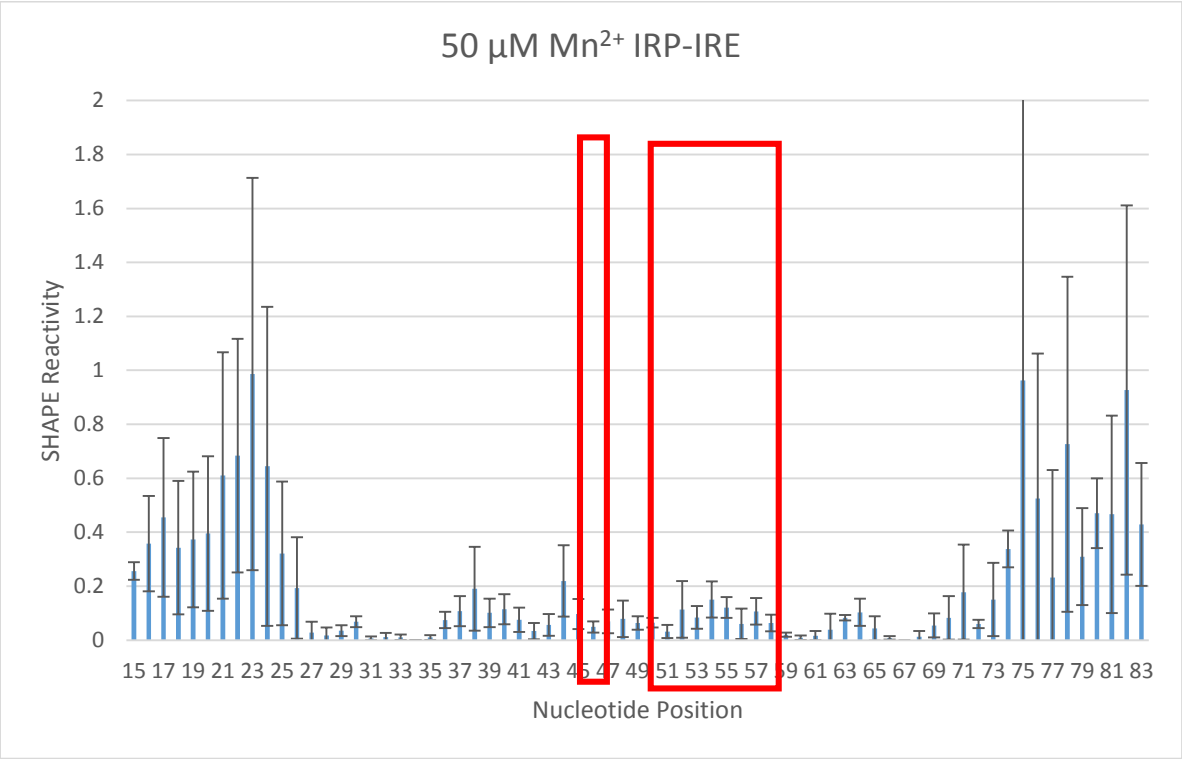

Graph 10. SHAPE Reactivity Histogram of IRE with IRP in 50 µM Mn^{2+}. The histogram is the average of three trials of the IRE-IRP complex in 50 µM Mn^{2+} hSHAPE data. The x-axis represents nucleotide position on the IRE. The highlighted region contains the nucleotides involved in IRP binding. Error bars were derived from standard deviations of the SHAPE reactivity data for each nucleotide.

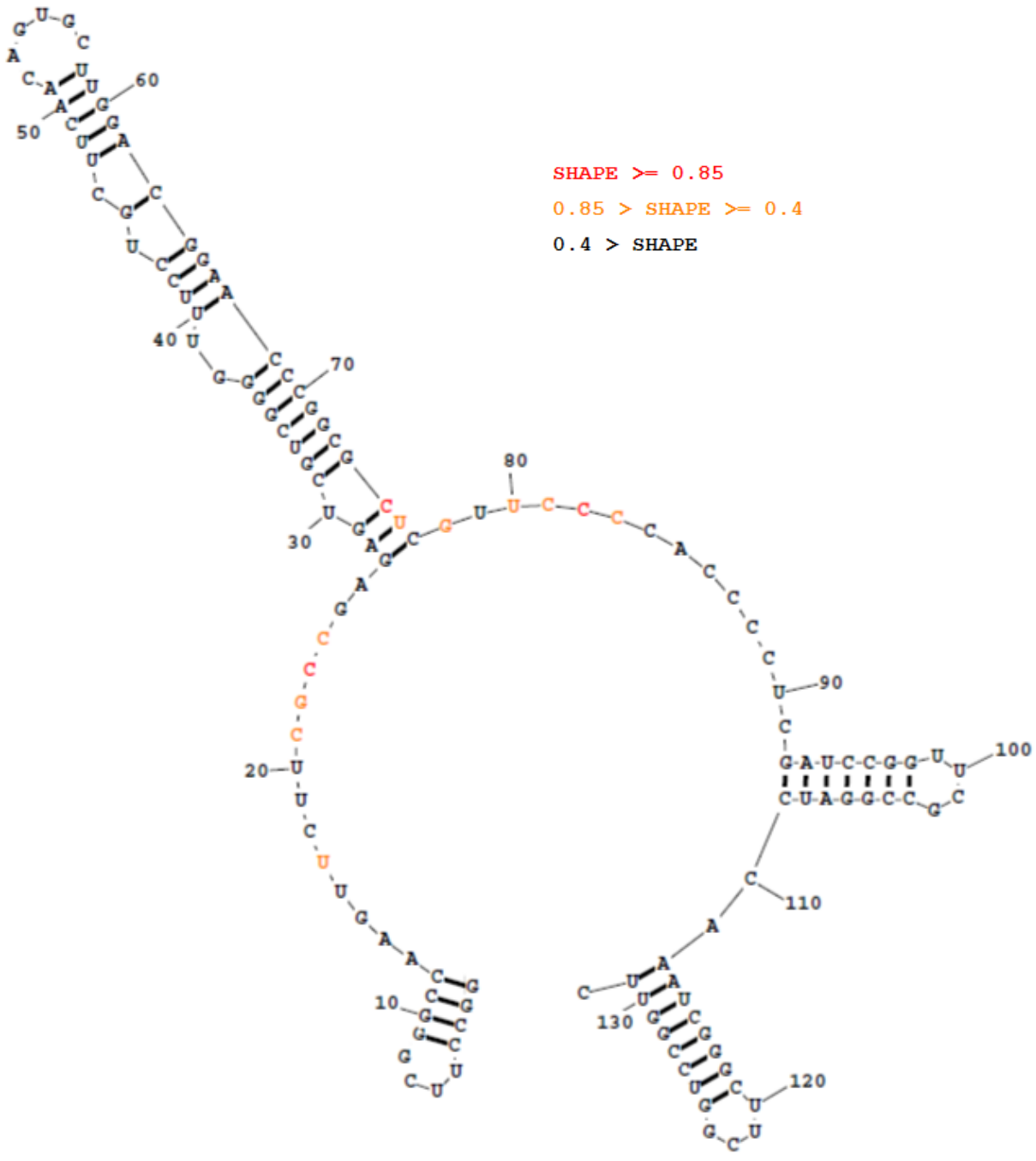

Figure 22. Predicted IRE Structure with IRP in 50 µM Mn^{2+}. The secondary structure was folded using RNAstructure software including free energy, nearest-neighbor parameters and the applied SHAPE reactivates for each nucleotide as pseudo-energy constraints. The highlighted loop region is the known area of IRP binding. The annotated shape scale is shown in the upper right corner. It must be noted that ~14nts at the 5' end and ~49nts at the 3' end, although colored black, did not have SHAPE reactivity data.

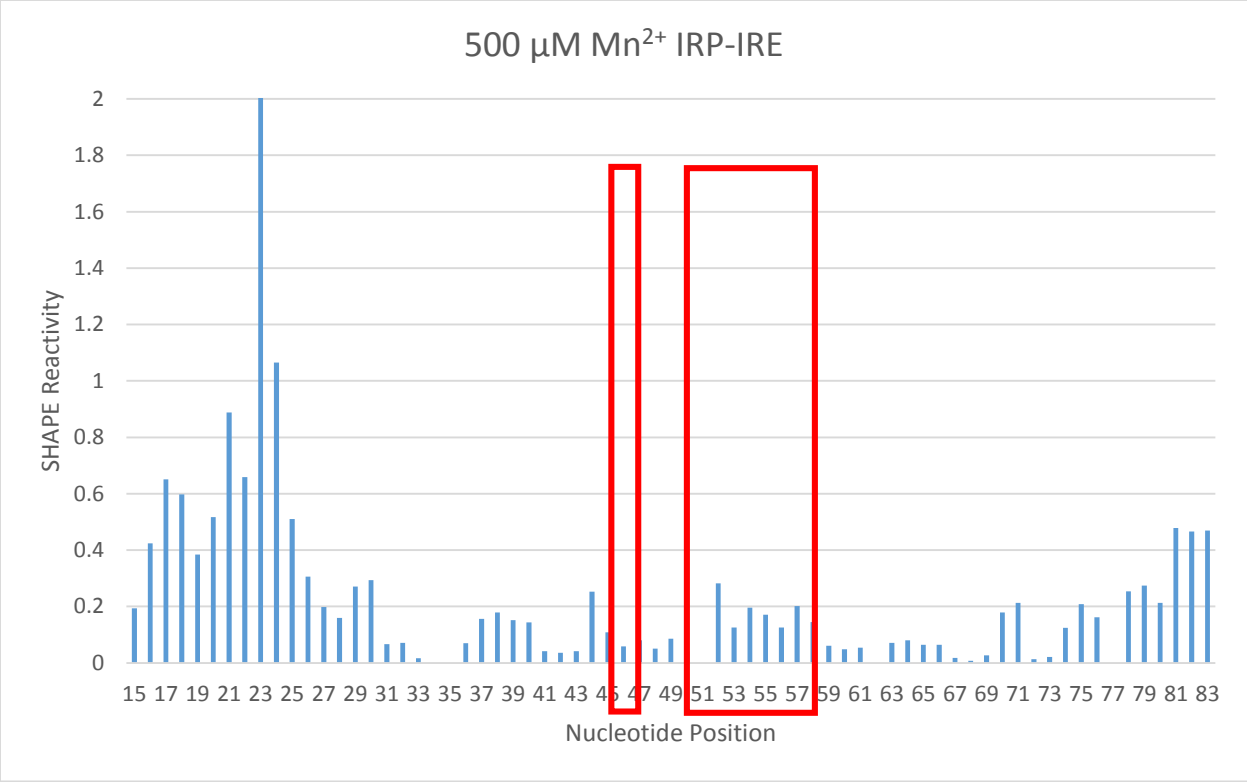

Graph 11. SHAPE Reactivity Histogram of IRE with IRP in 500 µM Mn^{2+}. The x-axis represents nucleotide position on the IRE. The highlighted regions contains the nucleotides involved in IRP binding. Error bars were not derived from standard deviations as there was only one successful experiment run at this concentration.

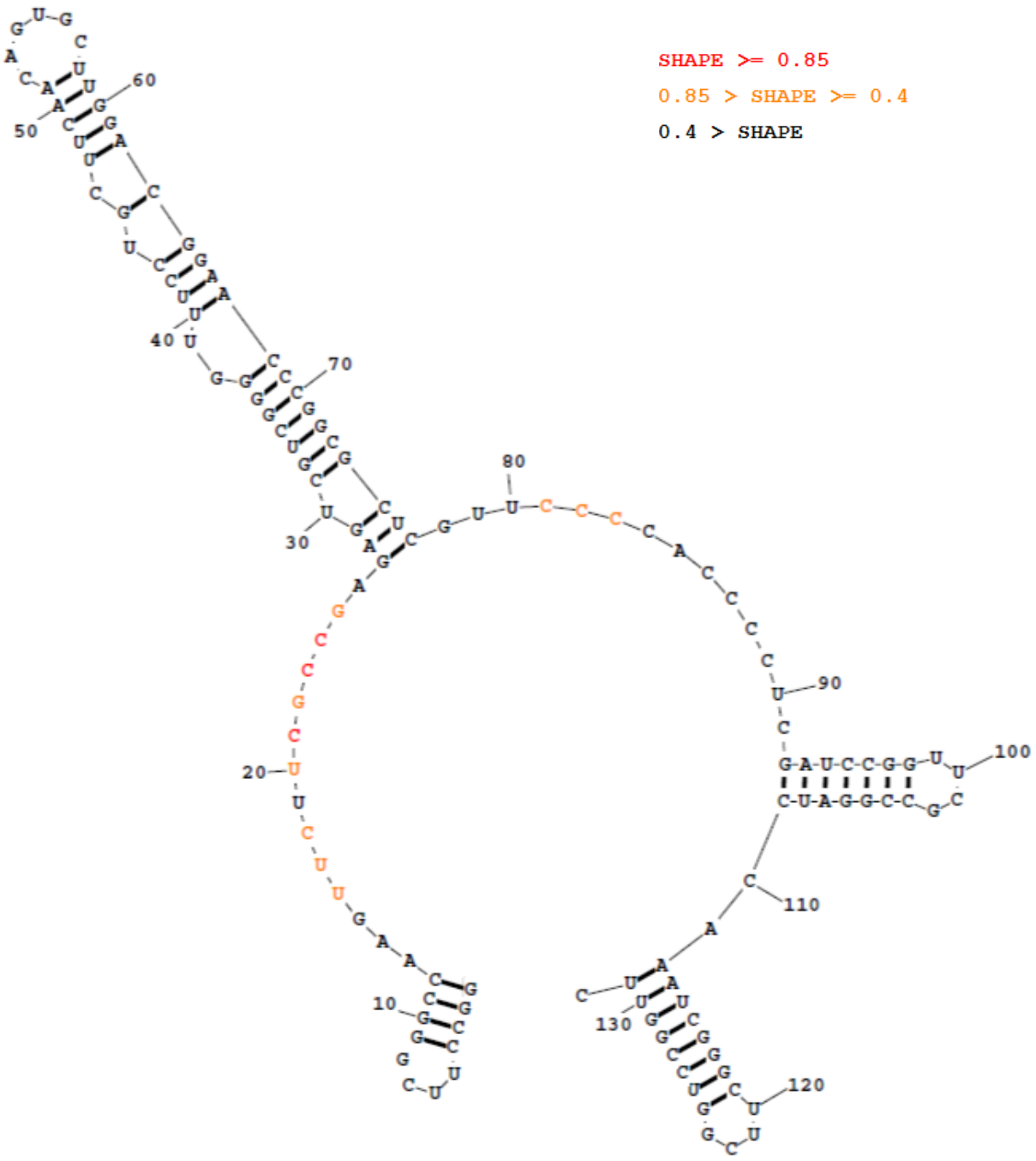

Figure 23. Predicted IRE Structure with IRP in 500 µM Mn^{2+}. The secondary structure was folded using RNAstructure software including free energy, nearest-neighbor parameters and the applied SHAPE reactivates for each nucleotide as pseudo-energy constraints. The highlighted loop region is the known area of IRP binding. The annotated shape scale is shown in the upper right corner. It must be noted that ~14nts at the 5' end and ~49nts at the 3' end, although colored black, did not have SHAPE reactivity data.

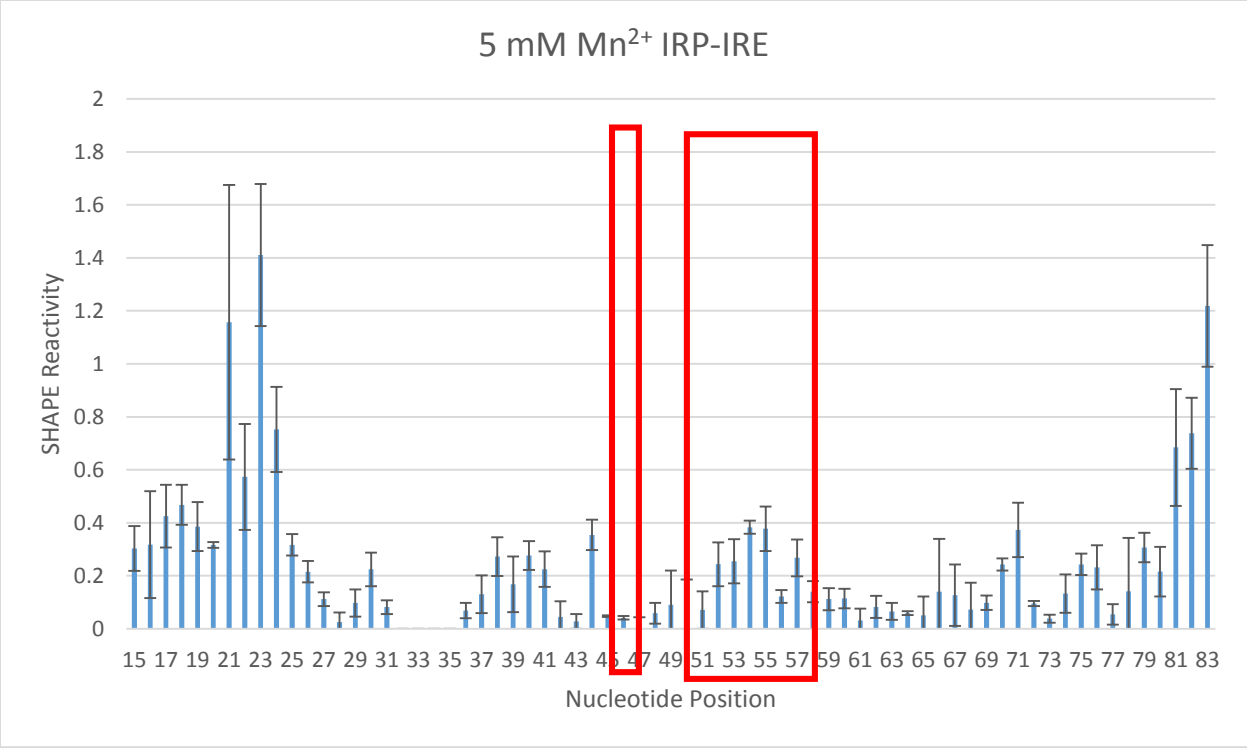

Graph 12. SHAPE Reactivity Histogram of IRE with IRP in 5 mM Mn^{2+}. The histogram is the average of two trials of the IRE-IRP complex in 5 mM Mn^{2+} hSHAPE data. The x-axis represents nucleotide position on the IRE. The highlighted region contains the nucleotides involved in IRP binding. Error bars were derived from standard deviations of the SHAPE reactivity data for each nucleotide.

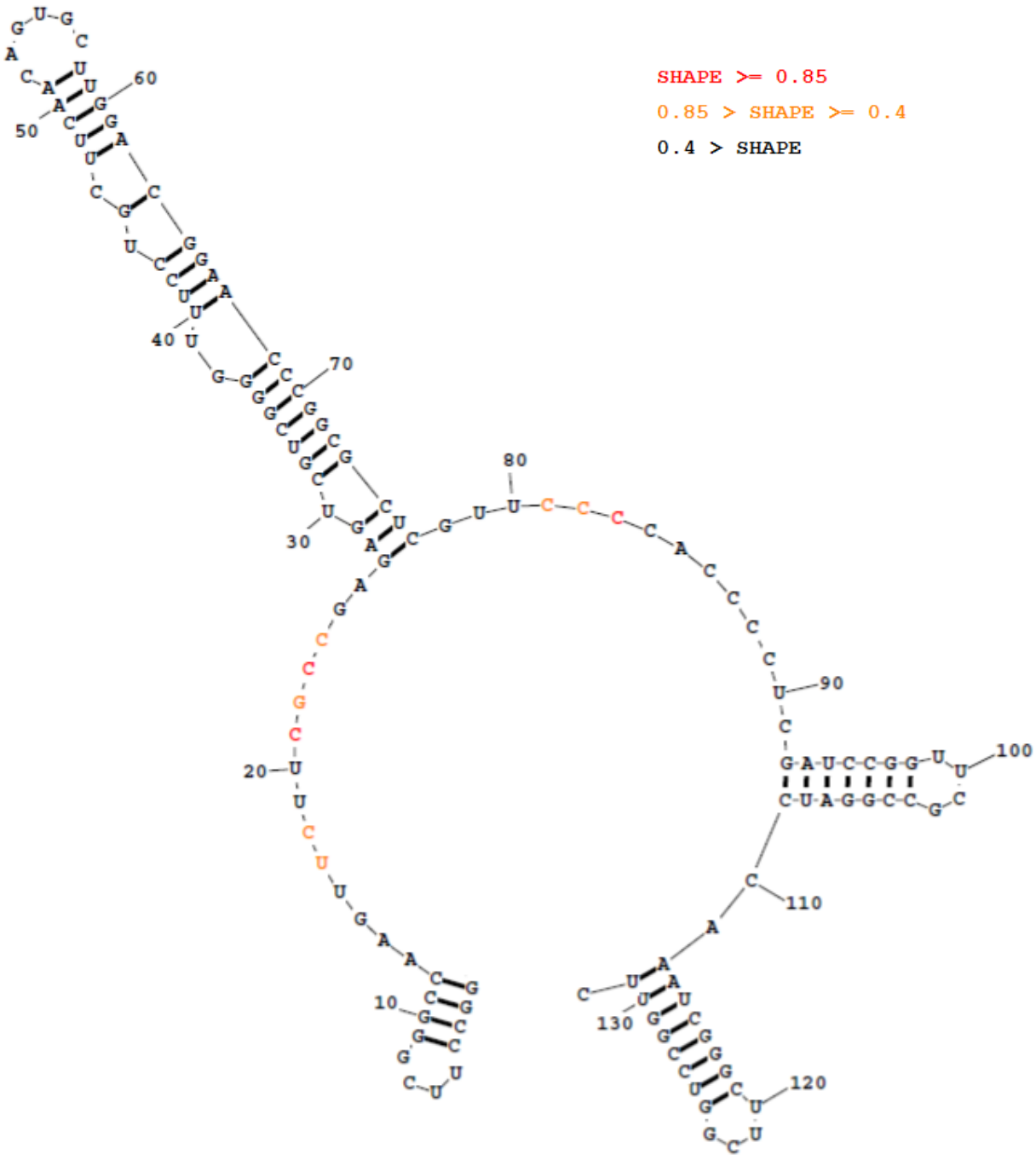

Figure 24. Predicted IRE Structure with IRP in 5 mM Mn^{2+}. The secondary structure was folded using RNAstructure software including free energy, nearest-neighbor parameters and the applied SHAPE reactivates for each nucleotide as pseudo-energy constraints. The highlighted loop region is the known area of IRP binding. The annotated shape scale is shown in the upper right corner. It must be noted that ~14nts at the 5' end and ~49nts at the 3' end, although colored black, did not have SHAPE reactivity data.

3.6 EMSA Mn^{2+} Pre-Incubation Experiments

Lastly, experiments were conducted observing Mn^{2+} influences on IRP-IRE complex association. In these experiments, Mn^{2+} was introduced to IRE and IRP separately before binding was allowed. These experiments were conducted only on EMSA 2% agarose gels. The resulting gels were then compared with gel experiments done using the Mn^{2+} dissociation method in order to observe Mn^{2+} effects on complex association, and also to see what component of the complex was being effected by Mn^{2+}.

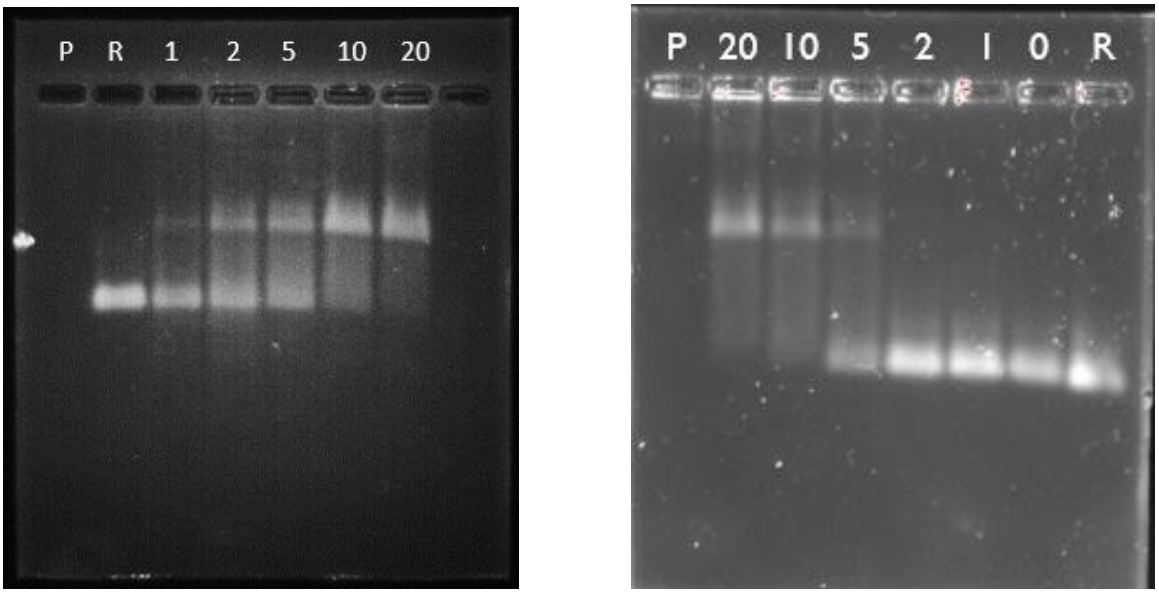

Figure 25. EMSA Control Gels. (A) EMSA control experiment with no Mn^{2+} present. Lanes P and R are IRP and IRE only respectively. The numbers atop the lanes represent the ratio of IRP:IRE (i.e. 20 = 20:1 IRP:IRE). (B) EMSA experiment dissociating the IRP-IRE complex in Mn^{2+} solution. Lane numbers are again representative of IRP:IRE ratios. The gel solutions were kept a constant 500 µM Mn^{2+}. Both gels were imaged as SYBR Green II RNA staining.

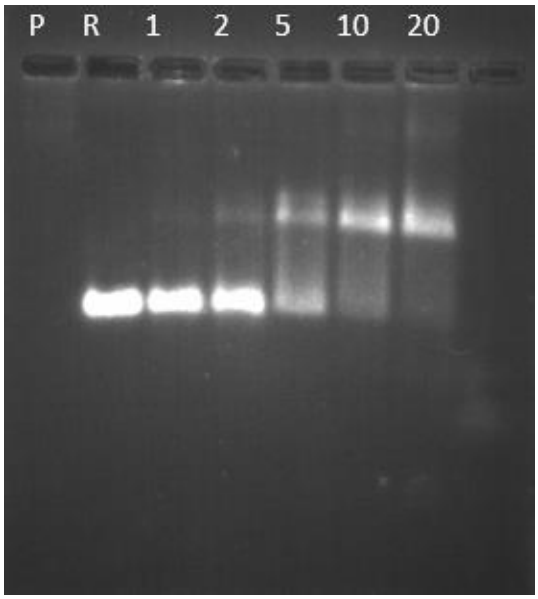

Figure 26. Pre-IRE and IRP Mn^{2+} Incubation Gel. The IRP and IRE were incubated in 500 µM Mn^{2+} prior to the IRP-IRE complex binding. Lane P and R are IRP only and IRE only respectively. The numbers at the top of each lane represent the IRP:IRE ratio. This gel image is the result of a SYBR Green II RNA staining.

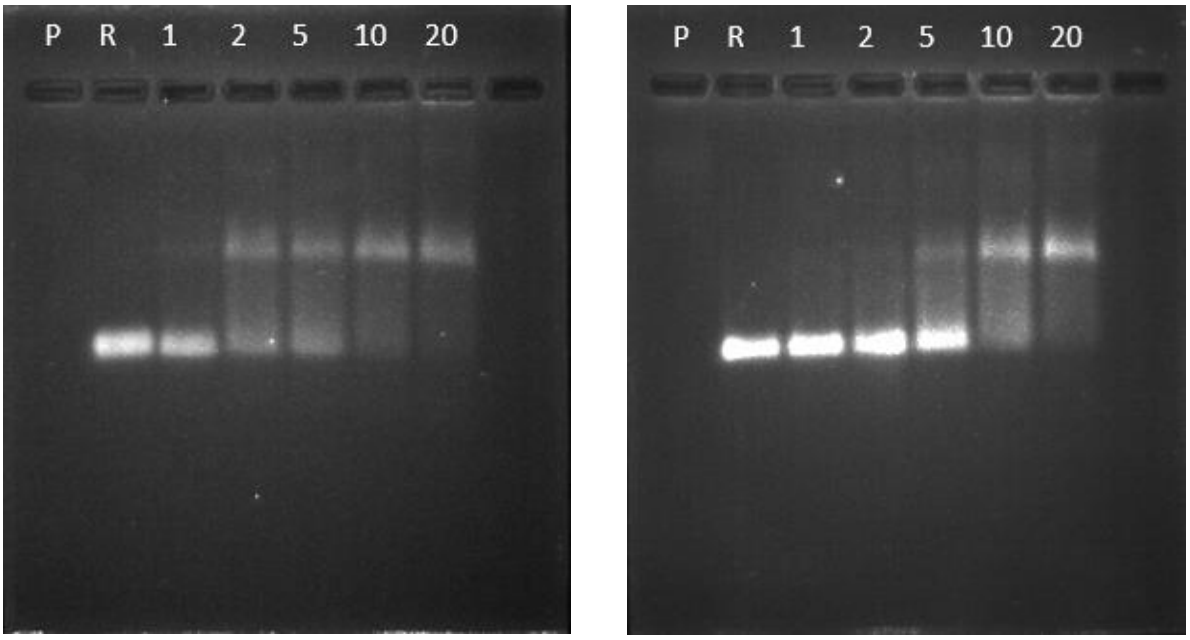

Figure 27. Pre-IRE only and Pre-IRP only Mn^{2+} Incubation Gel. (A) The EMSA gel on the left represents a similar pre-incubation method experiment; however, the IRE was incubated in 500 µM Mn^{2+} and the IRP was not. They were then brought together for binding. (B) Another EMSA gel similar to the gel on the left, however in this gel, only the IRP was incubated in 500 µM Mn^{2+} and the IRE was not. Again, both gel images were the result of SYBR Green II RNA staining.

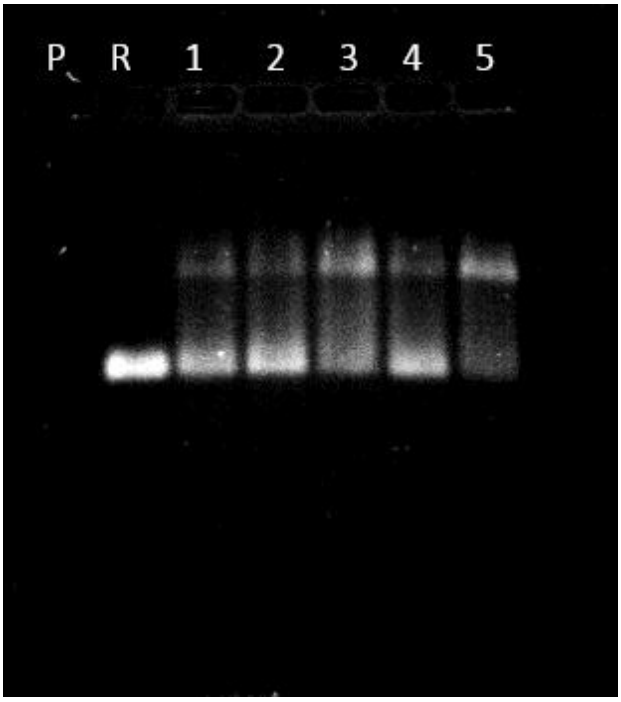

Figure 28. Combined Pre-Incubation Experiments 3:1 EMSA Gel. IRP:IRE ratios in this gel were kept at a constant 3:1 ratio. Lanes P and R were IRP only and IRE only respectively. Lane 1 is the IRP-IRE complex with no Mn^{2+} interference. Lane 2 is the IRP-IRE complex after both IRP and IRE were pre-incubated in 500 µM Mn^{2+} before binding. Lane 3 is the IRP-IRE complex after only the IRE was pre-incubated in 500 µM Mn^{2+}. Lane 4 is the IRP-IRE complex after only the IRP was pre-incubated in 500 µM Mn^{2+}. Lane 5 is IRP-IRE complex bound together before it was incubated with 500 µM Mn^{2+}. This gel is a result of SYBR Green II RNA staining, and its contrast and brightness have been uniformly changed before ImageJ software analysis.

Table 2. Standardized RNA Intensity Values of Mn^{2+} Pre-Incubation 3:1 EMSA Gel. The standardized values were obtained by dividing each intensity value as determined by ImageJ by the internal standard, the IRE only band in the R lane of Figure 28.

Unbound RNA	**0µM**	**Both Incubated**	**IRE Only Incubation**	**IRP only Incubation**	**Dissociation Method**
Standardized Values	0.595	0.684	0.372	0.599	0.219
Bound RNA	**0µM**	**Both Incubated**	**IRE Only Incubation**	**IRP only Incubation**	**Dissociation Method**
Standardized Values	0.130	0.084	0.278	0.123	0.336

CHAPTER 4

DISCUSSION

As previously mentioned, we wanted to observe IRP-IRE complex formation using each of our techniques before advancing toward experiments involving Mn^{2+} interferences. The EMSA gel experiment (Figure 14) shows that complex formation did occur. Not only did it occur, but the IRP successfully bound to each of our IRE RNAs (52, 77, and 132 nucleotides). Complex formation is quite distinctly represented by the upper bands of lanes 5-7 of the gel. Additionally, using a 10:1 ratio of IRP:IRE, the highly concentrated IRP solution bound up the majority of the IRE in lanes 5-7 also indicated efficient complex formation.

After confirming the binding of the IRP-IRE complex using EMSA methods, we wanted to observe complex formation through the changes in IRE SHAPE reactivates using our most sensitive technique, hSHAPE chemistry, again keeping IRP:IRE ratios at 10:1. This can be observed by comparing both Graphs 2 and 4, and Figures 15 and 16. In Graph 2, the IRE in binding buffer only, the highlighted regions in the red boxes indicate the nucleotides ($A^{53}G^{54}U^{55}$ and C^{46}) of the IRE that have been confirmed to bind to IRP.[8] When compared to the same highlighted regions in Graph 4, the IRP bound to IRE, there is a significant decrease in SHAPE reactivity levels, indicating the presence of a tertiary interacting with the IRE. This would be the IRP binding to the IRE. Additionally when observing the predicted structures (Figures 15 and 16), the nucleotides involved in IRP binding have high reactivity values in Figure 15 as indicated by the color coded annotated SHAPE reactivity scale; however, in Figure 16 these nucleotides drop from levels of high (red) and moderate (orange) SHAPE reactivity levels, to that of low to no SHAPE reactivity (black). Therefore, in comparing these graphs and figures, it was confirmed

via hSHAPE chemistry that the IRP-IRE complex forms. Also, it must be noted that the overall secondary structure of the IRE did not have any conformational changes.

In addition to confirming the IRP-IRE complex formation using hSHAPE chemistry, we also wanted to use this method to test IRP-mutant IRE binding. Previous studies indicated a weaker binding affinity off the IRP to the mutant IRE, thus we anticipated seeing this affect in the SHAPE reactivity values of the IRE binding nucleotides upon complex formation.[10] Again by comparing histograms (Graphs 6 and 8) and predicted secondary structures with colored SHAPE annotations (Figures 17 and 18), it can be seen that IRP-IRE complex formation does occur and is confirmed by the reduction in SHAPE reactivity values. Furthermore, the nucleotides involved in IRP binding that decreased in SHAPE reactivity values, had a decrease in values that was not as dramatic as that compared to the wild-type IRE hSHAPE experiments, therefore reaffirming that the mutant IRE has a weaker binding affinity to the IRP.

Once we had confirmed IRP-IRE complex formation using two of our techniques, we wanted to see if this complex formation could be translated into a physical representation using atomic force microscopy. By using the DNA dendron scaffold method as seen in the Materials and Methods section, we wanted to use AFM's z-height resolution capabilities to observe changes in z-heights indicating complex formation upon our gold-mica surface. Figure 19 shows the 1.6 micron scan and following line analysis profile of the first AFM images of just the G3 DNA dendron on the gold-mica surface. The line analysis shows the sizes of our DNA dendrons to be approximately 2-3 nm in height which corresponds with literature values.[28] The next scans were of the IRE complexed with the DNA dendron. These scans are not shown as the resulting images yielded no definitive increases in z-height as single stranded RNA has been shown to only have sizes of about 0.5 nm in AFM scans. Therefore we progressed to the next part of the

experiment by introducing the IRP to the solution. A previous group had done scanning force microscopy imaging on the IRP-IRE complex using a different construct and this group had found the IRP size to be approximately 2.5 nm in diameter.[29] Therefore we anticipated to see about a 2.5 nm increase in the sizes of the features on our gold-mica surface upon IRP addition. Figure 20 shows just this. The resulting line analysis profile shows the features to now be between 4-6 nm in height indicating complete DNA dendron-IRE-IRP complex formation.

After finding all three of our techniques could observe the formation of the complex, our group moved to interrogate the effects of Mn^{2+} on the dissociation of an already formed IRP-IRE complex. This dissociation method was first attempted during the AFM IRP-IRE binding experiments previously discussed. After the DNA dendron-IRE-IRP complex had been imaged, we introduced 500 µM Mn^{2+} to the solution and proceeded to image the surface. We anticipated seeing features on the surface now ranging only between 2-3 nm in z-height, indicating complex dissociation, observing only DNA dendrons and IRPs on the surface. However the resulting scans were of poor quality from the $MnCl_2$ addition causing large salt formations on the surface.

Next we decided to advance to use the EMSA gel technique to observe complex dissociation. The results of this experiment are shown in Figure 21. We performed a complete set of Mn^{2+} titration experiments on the complex with concentrations ranging from 50 µM up to 50 mM. We wanted to use the RNA fluorescence intensity data to plot a logarithmic curve and find the ½ $[Mn^{2+}]$ to use for the following hSHAPE chemistry IRP-IRE with Mn^{2+} experiments. We kept the IRP:IRE ratio at 10:1 for this experiment as well. By just observing Figure 21, it can be seen that the Mn^{2+} seemed to have little to no effect on the IRP-IRE complex dissociation, even at the highest concentrations. We decided to proceed and collect the ImageJ intensity values on the bound and unbound IRE for graphing purposes. The result of this graph is seen in Graph 9.

We had anticipated observing a graph with a relative decreasing slope; however, both plotted values and the derived best fit curve seems to be flat-line. With this result and an R^2 value of 35.5, it can be said that there is no correlation between the Mn^{2+} concentrations and the dissociation of the IRP-IRE complex.

In addition to the EMSA experiment, we wanted to continue to test the Mn^{2+} dissociation method with hSHAPE chemistry experiments. hSHAPE titrations were performed using a constant 10:1 IRP to IRE ratio and variable Mn^{2+} concentrations. Our goal was to plot titration curves and calculate $[Mn^{2+}]_{1/2,}$ the transition midpoint, at every nucleotide position in order to identify transition steps and predict Mn^{2+} binding sites. Using hSHAPE chemistry to achieve this has been previously done, for example, being used to analyze the effects of two ligands, Mg^{2+} and tobramycin (TOB^{5+}), on the folding of *S. cerevisiae* $tRNA^{Asp}$ transcripts, where it precisely confirmed the native structure of $tRNA^{Asp}$.[30] Based on the titration curves and the calculated $[ligand]_{1/2}$, the binding sites between both Mg^{2+} and TOB^{5+} to $tRNA^{Asp}$ were predicted.[30]

Therefore after successfully observing the IRP-IRE binding and its effects on the SHAPE reactivities of the IRE binding nucleotides using hSHAPE chemistry, we expected adverse effects. We hypothesized that there would be a gradual increase in SHAPE reactivities at the IRE binding nucleotides in the terminal loop region, and bulge regions upon the release of tertiary interactions with the IRP. However the results did not support this hypothesis, which can be seen in Graphs 10, 11, and 12 and Figures 22, 23, and 24. When compared to the SHAPE reactivities in these regions in the IRP-IRE hSHAPE experiment (Graph 4, Figure 16), the reactivities are relatively the same and the reactivities remained at low values (<0.4 on the annotated SHAPE scale).

In addition to the three Mn^{2+} concentrations illustrated in Figures 22-24, hSHAPE titrations of the 10:1 IRP-IRE complex were also performed at other Mn^{2+} concentrations (data not shown). We did not perform hSHAPE experiments at extremely high Mn^{2+} concentrations, such as 50 mM, as a previous study demonstrated a nonnegligible effect of higher concentrations of divalent metal ions on the final extent of 2'-*O*-adduct formation.[22]

In summary, EMSA and hSHAPE chemistry have been applied to determine the effects of Mn^{2+} on the dissociation of the IRE-IRP complex. The results from both techniques indicate that Mn^{2+} has little to no effect on the dissociation of the already bound IRE-IRP complex. Our experimental design for the titration of the IRE-IRP complex with Mn^{2+} was based on a model that suggests that Mn^{2+} binds only to the IRE RNA, and not to IRP.[11] If the model is incorrect, and if Mn^{2+} actually interacts with both IRP and the IRE RNA, or only with IRP, the experimental design using an IRP-IRE complex solution in a 10:1 molar ratio (i.e., IRP in large excess) would be invalid as small affects would be masked by the high IRP concentration.

In 2014, the Khan group published their kinetic studies of the effects of Mn^{2+} on the FTH IRE-IRP complex.[31] They found that Mn^{2+} ions induced about a six-fold decrease in the association rate of IRP binding to the FTH IRE RNA. In addition, Mn^{2+} induced approximately a two-fold increase in the dissociation rate of the IRP-IRE complex.

With this new information, we turned our focus from the effect of Mn^{2+} on dissociation of the IRP-IRE complex to the larger effect that Mn^{2+} has on the association between IRP and the IRE RNA. Concerned that the IRE RNA may not be the target of Mn^{2+}, or may not be the only target of Mn^{2+}, we designed the EMSA experiments, as described in the materials and methods section, to determine the target of the Mn^{2+}. The first experiment involved the pre-incubation of both the IRP and IRE in 500 μM Mn^{2+} run on a protein titration gel (Figure 26).

From these results, when compared to the control gel (Figure 25A), there is a clear increase in the intensity of the lower unbound RNA bands, especially at the lower ratios, in Figure 26. This led us to conclude that the Mn^{2+} was having an effect on complex association.

Next, we wanted to test whether the Mn^{2+} was affecting the IRP or the IRE in the complex. We ran protein titrations gels again, however we either pre-incubated only the IRE in Mn^{2+} (Figure 26A) or only the IRP in Mn^{2+} (Figure 26B). Upon comparison between these two figures with our control gel in Figure 25A, it is quite evident that the Mn^{2+} is appearing to have a significant effect on the IRP during pre-incubation, instead of the IRE. This result was concluded by the fluorescence intensity increases of the unbound RNA bands in the Pretreated-IRP gel but not in the Pretreated-IRE gel.

Lastly we wanted to make a direct comparison between the three pre-incubation methods on a single gel, while also including a control lane (with 0 µM Mn^{2+}) and a lane to compare to the previous dissociation method (complex formation followed by Mn^{2+} incubation). The results of this experiment are shown in Figure 28 and Table 2. Figure 28 displays greater intensities of the unbound RNA bands in the IRP-IRE pre-incubation lane and the IRP pre-incubation lane. After quantifying the data from the gel (Table 2), it is observed once again that the IRP-IRE pre-incubation lane, and the IRP pre-incubation lane had higher unbound RNA intensities. Additionally, the IRE pre-incubation lane had the second highest bound RNA intensity indicating Mn^{2+} had little to no effect on the IRE.

In brief, it can be postulated that the IRE-IRP complex is not highly affect by Mn^{2+} once bound; however, upon pre-incubation, it is the IRP that is affected and not the IRE as previously thought. Future considerations for this research must then involve shifting models to interrogating the IRP and the effect Mn^{2+} can have on it.

One highly recommended investigatory technique would be x-ray crystallography of the IRP upon Mn^{2+} interaction. This would provide us with the complete, atom-by-atom structure of the protein, including where the Mn^{2+} would be bound, and any conformational changes that have occurred in the protein.

Another technique that one could use for the protein is analytical ultracentrifugation (AUC). AUC is a technique that uses laser detection systems to analyze sedimentation upon high speed centrifugation. AUC has a sedimentation velocity in which the movement of solutes in high centrifugal fields uses hydrodynamic theory to define the size, shape, and interactions of macromolecules.[32] Additionally, AUC has a thermodynamic method called sedimentation equilibrium where equilibrium concentration gradients at lower centrifugal fields are analyzed to define molecular mass, assembly stoichiometry, association constants, and solution nonideality.[32] Essentially AUC will allow us to observe if there have been conformational changes to the protein under Mn^{2+} influences, but also we could use this technique to further study the IRP-IRE complex association and dissociation. Unlike x-ray crystallography, this technique could not tell us where exactly Mn^{2+} would be binding in the IRP.

We can also speculate as to where and how the Mn^{2+} is affecting the IRP. One thought, is that the Mn^{2+} could be assembling in a similar Fe-S cluster formation, and binding to the protein in that location, thus causing the IRP to shift to an ACO-1 conformation. This could be a result of Cys^- side chains having more favorable charge-charge interactions with metal ions.[33] As discussed in the introduction, the 4Fe-4S cluster is bound to three Cys amino acids of the IRP. Additionally, "soft" metal ions such as Fe^{2+} and Mn^{2+} will frequently bind to weak field ligands such as sulfur, which is in the side chain of cysteine.[34]

CHAPTER 5

CONCLUSIONS

In conclusion, our group was able to successfully confirm the formation of the IRP-IRE complex using EMSA gels, hSHAPE chemistry, and atomic force microscopy. Due to these results we were able to pursue further investigations of the complex, following the model that Mn^{2+} had the ability to dissociate the complex, specifically affecting the IRE. After several experiments both with EMSA gels and hSHAPE chemistry, we were able to conclude that Mn^{2+} had little to no effect on the dissociation of the IRP-IRE complex. Therefore we adjusted our model to correspond with an updated version indicating that the metal ion will have a greater effect on association than dissociation. Our EMSA Mn^{2+} pre-incubation experiments not only confirm this, but also indicate that the Mn^{2+} is having a larger effect on the IRP component of the complex. From here, future experimentation would need to be conducted to assess the effects that Mn^{2+} is having on the IRP.

REFERENCES

1. Theil, E. C., Ferritin: structure, gene regulation, and cellular function in animals, plants, and microorganisms. *Annual review of biochemistry* **1987,** *56* (1), 289-315.
2. Theil, E. C., Ferritin: the protein nanocage and iron biomineral in health and in disease. *Inorganic chemistry* **2013,** *52* (21), 12223-12233.
3. Honarmand Ebrahimi, K.; Bill, E.; Hagedoorn, P.-L.; Hagen, W. R., The catalytic center of ferritin regulates iron storage via Fe(II)-Fe(III) displacement. *Nat Chem Biol* **2012,** *8* (11), 941-948.
4. Carmona, U.; Li, L.; Zhang, L.; Knez, M., Ferritin light-chain subunits: key elements for the electron transfer across the protein cage. *Chemical communications (Cambridge, England)* **2014,** *50* (97), 15358-61.
5. Volz, K., The functional duality of iron regulatory protein 1. *Current opinion in structural biology* **2008,** *18* (1), 106-11.
6. Dupuy, J.; Volbeda, A.; Carpentier, P.; Darnault, C.; Moulis, J. M.; Fontecilla-Camps, J. C., Crystal structure of human iron regulatory protein 1 as cytosolic aconitase. *Structure (London, England : 1993)* **2006,** *14* (1), 129-39.
7. Brazzolotto, X.; Timmins, P.; Dupont, Y.; Moulis, J. M., Structural changes associated with switching activities of human iron regulatory protein 1. *The Journal of biological chemistry* **2002,** *277* (14), 11995-2000.
8. Walden, W. E.; Selezneva, A. I.; Dupuy, J.; Volbeda, A.; Fontecilla-Camps, J. C.; Theil, E. C.; Volz, K., Structure of dual function iron regulatory protein 1 complexed with ferritin IRE-RNA. *Science (New York, N.Y.)* **2006,** *314* (5807), 1903-8.
9. Joshi, R.; Morán, E.; Sánchez, M., Cellular iron metabolism. The IRP/IRE regulatory network. *Iron Metabolism* **2012**, 25-58.
10. Kato, J.; Fujikawa, K.; Kanda, M.; Fukuda, N.; Sasaki, K.; Takayama, T.; Kobune, M.; Takada, K.; Takimoto, R.; Hamada, H.; Ikeda, T.; Niitsu, Y., A mutation, in the iron-responsive element of H ferritin mRNA, causing autosomal dominant iron overload. *American journal of human genetics* **2001,** *69* (1), 191-7.
11. Khan, M. A.; Walden, W. E.; Goss, D. J.; Theil, E. C., Direct Fe2+ sensing by iron-responsive messenger RNA:repressor complexes weakens binding. *The Journal of biological chemistry* **2009,** *284* (44), 30122-8.
12. Ma, J.; Haldar, S.; Khan, M. A.; Sharma, S. D.; Merrick, W. C.; Theil, E. C.; Goss, D. J., Fe2+ binds iron responsive element-RNA, selectively changing protein-binding affinities and regulating mRNA repression and activation. *Proceedings of the National Academy of Sciences of the United States of America* **2012,** *109* (22), 8417-22.
13. Tibodeau, J. D.; Fox, P. M.; Ropp, P. A.; Theil, E. C.; Thorp, H. H., The up-regulation of ferritin expression using a small-molecule ligand to the native mRNA. *Proceedings of the National Academy of Sciences of the United States of America* **2006,** *103* (2), 253-7.
14. Canzoneri, J. C.; Oyelere, A. K., Interaction of anthracyclines with iron responsive element mRNAs. *Nucleic acids research* **2008,** *36* (21), 6825-34.
15. Ryder, S. P.; Recht, M. I.; Williamson, J. R., Quantitative analysis of protein-RNA interactions by gel mobility shift. *Methods in molecular biology (Clifton, N.J.)* **2008,** *488*, 99-115.

16. Heffler, M. A.; Walters, R. D.; Kugel, J. F., Using electrophoretic mobility shift assays to measure equilibrium dissociation constants: GAL4-p53 binding DNA as a model system. *Biochemistry and molecular biology education : a bimonthly publication of the International Union of Biochemistry and Molecular Biology* **2012,** *40* (6), 383-7.
17. Gross, L.; Mohn, F.; Moll, N.; Liljeroth, P.; Meyer, G., The chemical structure of a molecule resolved by atomic force microscopy. *Science (New York, N.Y.)* **2009,** *325* (5944), 1110-4.
18. Gross, L.; Mohn, F.; Moll, N.; Schuler, B.; Criado, A.; Guitian, E.; Pena, D.; Gourdon, A.; Meyer, G., Bond-order discrimination by atomic force microscopy. *Science (New York, N.Y.)* **2012,** *337* (6100), 1326-9.
19. Hansma, H. G.; Sinsheimer, R. L.; Li, M. Q.; Hansma, P. K., Atomic force microscopy of single- and double-stranded DNA. *Nucleic acids research* **1992,** *20* (14), 3585-90.
20. Zhu, J.; Feng, X.; Lou, J.; Li, W.; Li, S.; Zhu, H.; Yang, L.; Zhang, A.; He, L.; Li, C., Accurate quantification of microRNA via single strand displacement reaction on DNA origami motif. *PloS one* **2013,** *8* (8), e69856.
21. Day, B. S.; Fiegland, L. R.; Vint, E. S.; Shen, W.; Morris, J. R.; Norton, M. L., Thiolated dendrimers as multi-point binding headgroups for DNA immobilization on gold. *Langmuir : the ACS journal of surfaces and colloids* **2011,** *27* (20), 12434-42.
22. Mortimer, S. A.; Weeks, K. M., A fast-acting reagent for accurate analysis of RNA secondary and tertiary structure by SHAPE chemistry. *Journal of the American Chemical Society* **2007,** *129* (14), 4144-5.
23. Mathews, D. H.; Disney, M. D.; Childs, J. L.; Schroeder, S. J.; Zuker, M.; Turner, D. H., Incorporating chemical modification constraints into a dynamic programming algorithm for prediction of RNA secondary structure. *Proceedings of the National Academy of Sciences of the United States of America* **2004,** *101* (19), 7287-92.
24. Merino, E. J.; Wilkinson, K. A.; Coughlan, J. L.; Weeks, K. M., RNA structure analysis at single nucleotide resolution by selective 2'-hydroxyl acylation and primer extension (SHAPE). *Journal of the American Chemical Society* **2005,** *127* (12), 4223-31.
25. Karabiber, F.; McGinnis, J. L.; Favorov, O. V.; Weeks, K. M., QuShape: rapid, accurate, and best-practices quantification of nucleic acid probing information, resolved by capillary electrophoresis. *RNA (New York, N.Y.)* **2013,** *19* (1), 63-73.
26. Vasa, S. M.; Guex, N.; Wilkinson, K. A.; Weeks, K. M.; Giddings, M. C., ShapeFinder: a software system for high-throughput quantitative analysis of nucleic acid reactivity information resolved by capillary electrophoresis. *RNA (New York, N.Y.)* **2008,** *14* (10), 1979-90.
27. Reuter, J. S.; Mathews, D. H., RNAstructure: software for RNA secondary structure prediction and analysis. *BMC bioinformatics* **2010,** *11*, 129.
28. Hierlemann, A.; Campbell, J. K.; Baker, L. A.; Crooks, R. M.; Ricco, A. J., Structural distortion of dendrimers on gold surfaces: a tapping-mode AFM investigation. *Journal of the American Chemical Society* **1998,** *120* (21), 5323-5324.
29. Bonin, M.; Oberstrass, J.; Vogt, U.; Wassenegger, M.; Nellen, W., Binding of IRE-BP to its cognate RNA sequence: SFM studies on a universal RNA backbone for the analysis of RNA-protein interaction. *Biological chemistry* **2001,** *382* (8), 1157-62.
30. Wang, B.; Wilkinson, K. A.; Weeks, K. M., Complex ligand-induced conformational changes in tRNA(Asp) revealed by single-nucleotide resolution SHAPE chemistry. *Biochemistry* **2008,** *47* (11), 3454-61.

31. Khan, M. A.; Ma, J.; Walden, W. E.; Merrick, W. C.; Theil, E. C.; Goss, D. J., Rapid kinetics of iron responsive element (IRE) RNA/iron regulatory protein 1 and IRE-RNA/eIF4F complexes respond differently to metal ions. *Nucleic acids research* **2014,** *42* (10), 6567-77.
32. Cole, J. L.; Lary, J. W.; Moody, T.; Laue, T. M., Analytical Ultracentrifugation: Sedimentation Velocity and Sedimentation Equilibrium. *Methods in cell biology* **2008,** *84*, 143-79.
33. Dudev, T.; Lim, C., Competition among metal ions for protein binding sites: determinants of metal ion selectivity in proteins. *Chemical reviews* **2013,** *114* (1), 538-556.
34. Yamashita, M. M.; Wesson, L.; Eisenman, G.; Eisenberg, D., Where metal ions bind in proteins. *Proceedings of the National Academy of Sciences* **1990,** *87* (15), 5648-5652.

APPENDIX A: IRB LETTER OF APPROVAL

MARSHALL UNIVERSITY®
www.marshall.edu

Office of Research Integrity

May 8, 2015

Dr. Bin Wang
Department of Chemistry
1 John Marshall Dr.
Huntington WV, 25755

Dear Dr. Wang:

This letter is in response to the submitted thesis abstract for Eric T. Mendenhall entitled *"An Investigation of the Effect of MN2+ on the FTH1 IRE-IRP Complex."* After assessing the abstract it has been deemed not to be human subject research and therefore exempt from oversight of the Marshall University Institutional Review Board (IRB). The Code of Federal Regulations (45CFR46) has set forth the criteria utilized in making this determination. Since the information in this study does not involve human subjects as defined in the above referenced instruction it is not considered human subject research. If there are any changes to the abstract you provided then you would need to resubmit that information to the Office of Research Integrity for review and a determination.

I appreciate your willingness to submit the abstract for determination. Please feel free to contact the Office of Research Integrity if you have any questions regarding future protocols that may require IRB review.

Sincerely,

Bruce F. Day, ThD, CIP
Director